
# NAVAL POSTGRADUATE SCHOOL

**MONTEREY, CALIFORNIA**

# THESIS

**OPTIMAL PLACEMENT OF NON-INTRUSIVE WASTE HEAT RECOVERY DEVICES IN EXHAUST DUCTS**

by

Ryan S. Bohning

June 2015

Thesis Advisor: Sanjeev B. Sathe
Co-Advisor: Garth V. Hobson

**Approved for public release; distribution is unlimited**

***Reissued 26 Aug to correct math symbol mechanical mistranslations throughout.***

THIS PAGE INTENTIONALLY LEFT BLANK

# REPORT DOCUMENTATION PAGE

*Form Approved OMB No. 0704–0188*



| **1. AGENCY USE ONLY** *(Leave blank)* | **2. REPORT DATE** June 2015 | **3. REPORT TYPE AND DATES COVERED** Master's Thesis |
|---|---|---|

**4. TITLE AND SUBTITLE**
OPTIMAL PLACEMENT OF NON-INTRUSIVE WASTE HEAT RECOVERY DEVICES IN EXHAUST DUCTS

**5. FUNDING NUMBERS**

**6. AUTHOR(S)** Bohning, Ryan S.

**7. PERFORMING ORGANIZATION NAME(S) AND ADDRESS(ES)**
Naval Postgraduate School
Monterey, CA 93943–5000

**8. PERFORMING ORGANIZATION REPORT NUMBER**

**9. SPONSORING /MONITORING AGENCY NAME(S) AND ADDRESS(ES)**
Office of Naval Research

**10. SPONSORING/MONITORING AGENCY REPORT NUMBER**

**11. SUPPLEMENTARY NOTES** The views expressed in this thesis are those of the author and do not reflect the official policy or position of the Department of Defense or the U.S. Government. IRB Protocol number ____N/A____.

**12a. DISTRIBUTION / AVAILABILITY STATEMENT**
Approved for public release; distribution is unlimited

**12b. DISTRIBUTION CODE**

**13. ABSTRACT (maximum 200 words)**

The Secretary of the Navy has ordered the U.S. Navy and Marine Corps to reduce energy usage. This study explores how to optimize placement and size of a non-intrusive waste heat recovery device for energy recovery in exhaust ducts. Additionally, it explores the effect that a device has on the exhaust infrared signature by analyzing the change in the bulk temperature at the exhaust outlet.

Optimal device placement and size is dependent on duct geometry, external heat transfer coefficient, and flow characteristics, namely Reynolds number. Infrared signature intensity reductions of 1–14% are only achievable with unpractically long thermoelectric generator devices and high external heat transfer coefficients. Doubling the external heat transfer coefficient increases heat recovery by 15–30% for low Reynolds number flows ($10^4$) and 75–90% for high Reynolds number flows ($10^5$~$10^6$).

In low Reynolds number flows (~$10^4$), device position can account for a 75% change in energy recovery whereas high Reynolds number flows (~$10^6$) have unexpected areas of higher heat transfer. Position changes can increase heat recovery 10–70%, while increasing device size may only marginally improve results. Identifying local maxima for heat transfer, especially in high Reynolds number flows (~$10^6$), is counterintuitive because of unexpected recirculation zone effects.

**14. SUBJECT TERMS**
Waste heat recovery, thermoelectric generator, optimization, IR signature, heat transfer, thermal stress

**15. NUMBER OF PAGES**
103

**16. PRICE CODE**

| **17. SECURITY CLASSIFICATION OF REPORT** | **18. SECURITY CLASSIFICATION OF THIS PAGE** | **19. SECURITY CLASSIFICATION OF ABSTRACT** | **20. LIMITATION OF ABSTRACT** |
|---|---|---|---|
| Unclassified | Unclassified | Unclassified | UU |

NSN 7540–01–280–5500

Standard Form 298 (Rev. 2–89)
Prescribed by ANSI Std. 239–18

THIS PAGE INTENTIONALLY LEFT BLANK

**Approved for public release; distribution is unlimited**

# OPTIMAL PLACEMENT OF NON-INTRUSIVE WASTE HEAT RECOVERY DEVICES IN EXHAUST DUCTS

Ryan S. Bohning
Lieutenant, United States Navy
B.S.M.E, United States Naval Academy, 2007

Submitted in partial fulfillment of the
requirements for the degree of

**MASTER OF SCIENCE IN MECHANICAL ENGINEERING**

from the

**NAVAL POSTGRADUATE SCHOOL**
**June 2015**

Author: Ryan S. Bohning

Approved by: Sanjeev B. Sathe
Thesis Advisor

Garth V. Hobson
Co-Advisor

Garth V. Hobson
Chair, Department of Mechanical and Aerospace Engineering

THIS PAGE INTENTIONALLY LEFT BLANK

# ABSTRACT

The Secretary of the Navy has ordered the U.S. Navy and Marine Corps to reduce energy usage. This study explores how to optimize placement and size of a non-intrusive waste heat recovery device for energy recovery in exhaust ducts. Additionally, it explores the effect that a device has on the exhaust infrared signature by analyzing the change in the bulk temperature at the exhaust outlet.

Optimal device placement and size is dependent on duct geometry, external heat transfer coefficient, and flow characteristics, namely Reynolds number. Infrared signature intensity reductions of 1–14% are only achievable with unpractically long thermoelectric generator devices and high external heat transfer coefficients. Doubling the external heat transfer coefficient increases heat recovery by 15–30% for low Reynolds number flows ($10^4$) and 75–90% for high Reynolds number flows ($10^5$~$10^6$).

In low Reynolds number flows (~$10^4$), device position can account for a 75% change in energy recovery whereas high Reynolds number flows (~$10^6$) have unexpected areas of higher heat transfer. Position changes can increase heat recovery 10–70%, while increasing device size may only marginally improve results. Identifying local maxima for heat transfer, especially in high Reynolds number flows (~$10^6$), is counterintuitive because of unexpected recirculation zone effects.

THIS PAGE INTENTIONALLY LEFT BLANK

# TABLE OF CONTENTS

# LIST OF FIGURES

THIS PAGE INTENTIONALLY LEFT BLANK

# LIST OF TABLES

THIS PAGE INTENTIONALLY LEFT BLANK

# LIST OF ACRONYMS AND ABBREVIATIONS

| | |
|---|---|
| 2-D | two-dimensional |
| 3-D | three-dimensional |
| ACAT | Acquisition category |
| Allison 501K | Shipboard gas turbine generator |
| CFD | Computational fluid dynamics |
| DoD | Department of Defense |
| DON | Department of the Navy |
| E2O | Marine Corps Expeditionary Energy Office |
| ExFOB | Experimental Forward Operating Base |
| FLIR | Forward-looking infrared |
| IR | Infrared |
| LM100 | Shore-based gas turbine generator |
| LM2500 | Shipboard gas turbine prime mover |
| MEP-803A | USMC diesel generator set |
| MT-30 | Shipboard gas turbine prime mover |
| NPS | Naval Postgraduate School |
| ONR | Office of Naval Research |
| SBIR | Small Business Innovation Research |
| S-$CO_2$ | Supercritical carbon dioxide |
| SECNAV | Secretary of the Navy |
| TEG | Thermoelectric generator |
| USMC | United States Marine Corps |
| USN | United States Navy |
| WHR | Waste heat recovery |
| WHRS | Waste heat recovery system |

THIS PAGE INTENTIONALLY LEFT BLANK

# NOMENCLATURE

| Symbols | Equation | Description | Units |
|---|---|---|---|
| $C_p$ or $c_p$ | | Specific heat (const. p) | [J/(kgK)] |
| d | | Distance between duct walls | [m] |
| $D_h$ | 2d | Hydraulic diameter | [m] |
| $E_{\lambda,b}$ | $\frac{C_1}{\lambda^5\left[e^{(C_2/\lambda T)}-1\right]}$ | Spectral emissive power | $[W/m^2\ \mu m]$ |
| e | | Internal energy | [J/kg] |
| Gz | $\frac{D_h}{x}\mathrm{Re}\,\mathrm{Pr}$ | Graetz number | |
| H* | $H/D_h$ | Non-dimensional duct height | |
| h | e+pv | Enthalpy | [J/kg] |
| h | | Heat transfer coefficient | $[W/(m^2K)]$ |
| $h_{ext}^{*}$ | $\frac{h_{ext}}{\dot{m}C_P/A_c}$ | Non-dimensional external heat transfer coefficient | |
| k | | Thermal conductivity | $[W/(mK)]$ |
| $k$ | | Turbulent kinetic energy | |
| L* | $L/D_h$ | Non-dimensional duct length | |
| L* | $l/D_h$ | Non-dimensional device length | |
| Ma | | Mach number | |
| $\dot{m}$ or $m_{dot}$ | $\rho A_c \bar{U}$ | Mass flow rate | [kg/s] |
| Nu | $\frac{hD_h}{k}$ | Nusselt number | |
| p | | Pressure | [Pa] |

| Symbols | Equation | Description | Units |
|---|---|---|---|
| Pr | $\frac{C_p \mu}{k}$ | Prandtl number | |
| Q | | Heat | [W] |
| $Q_1$ | | Heat transfer through top horizontal wall of backwards L duct | [W] |
| $Q_2$ | | Heat transfer through bottom horizontal wall of backwards L duct | [W] |
| $Q_3$ | | Heat transfer through left vertical wall of backwards L | [W] |
| $Q_4$ | | Heat transfer through right vertical wall of backwards L duct | [W] |
| Q** | $\frac{Q_{wall}}{\dot{m} C_p (T_0 - T_\infty)}$ | Non-dimensional heat transfer | |
| q'' | $h_{ext}(T_w - T_\infty)$ | Heat flux through wall | [W/m$^2$] |
| Re | $\frac{\rho \bar{U} D_h}{\mu}$ | Reynolds number | |
| $S_M$ | | Momentum source | [N/m$^3$] |
| $S_E$ | | Energy source | [W/m$^3$] |
| s* | (x**,y**) | Non-dimensional perimeter distance | |
| T | | Temperature | [K] |
| $T_0$ | | Inlet temperature | [K] |

| Symbols | Equation | Description | Units |
|---|---|---|---|
| $T_b$ | $\frac{\int_{A_c} \rho(x,y)u(x,y)T(x,y)\,dA_c}{\dot{m}}$ | Bulk temperature | [K] |
| $T_{nw}$ | | Near-wall temperature | [K] |
| $T_w$ | | Wall temperature | [K] |
| $T_\infty$ | | Ambient temperature | [K] |
| t | | Time or wall thickness | [s] or [m] |
| t* | | Non-dimensional duct thickness | |
| $\bar{U}$ | | Mean velocity | [m/s] |
| $\vec{U}$ | | Velocity (vector) | [m/s] |
| U | $1/(t/k_{wall}+1/h_{ext})$ | Overall external heat transfer coefficient. Includes wall thermal conductivity and external heat transfer coefficient. | $[W/(m^2K)]$ |
| u | | Velocity (scalar) | [m/s] |
| u* | $u/\bar{U}$ | Non-dimensional velocity | |
| v | | Specific volume | $[m^3/kg]$ |
| x* | $\frac{(x/D_h)}{\mathrm{Re}\,\mathrm{Pr}} = Gz^{-1}$ | Inverse Graetz number | |
| x** and y** | $\frac{x}{D_h}\frac{D_h}{L} = \frac{x}{L}$<br>$\frac{y}{D_h}\frac{D_h}{L} = \frac{y}{L}$ | Non-dimensional distance in flow direction | |
| $\epsilon$ | | Turbulent dissipation | |
| $\zeta^*$ | $\frac{H}{L}$ | Ratio of non-dimensional | |

| Symbols | Equation | Description | Units |
|---|---|---|---|
| $\Theta$ | $\frac{q''}{q''_{max}}$ | Non-dimensional heat flux | |
| $\theta$ | $\frac{T-T_\infty}{T_0-T_\infty}$ | Non-dimensional temperature drop | |
| | | duct height to length | |
| $\lambda$ | | Wavelength | [ $\mu m$ ] |
| $\rho$ | | Density | [kg/m$^3$] |
| $\tau$ | | Stress tensor | [Pa] |

# ACKNOWLEDGMENTS

I would like to first and foremost thank God for blessing me with the strength and illumination to complete this thesis.

Thank you so much to my loving wife, Jessica, and my four beautiful daughters, Laney, Kinzley, Zoe, and Allison, for supporting me through not just this thesis but through the completion of two Master's degrees, both of which required travel away from home on several occasions. I really could not have done this without them. Thanks, girls, for understanding that Daddy had long days and couldn't play, and thank you, Jess, for always believing in me.

It goes without saying that my thesis advisor, Dr. Sathe, was a true inspiration to me. A wonderful coach, he helped me to persevere through my toughest times at NPS; and that experience of perseverance and triumph truly is one of life's greatest lessons. Thank you.

Lastly, thanks to all my colleagues and friends who are too numerous to name here, who provided support and guidance during my time at NPS. Also, thanks to Mom, Dad, Tyler, Darrell, and Kathy for always being there to listen and encourage me.

THIS PAGE INTENTIONALLY LEFT BLANK

# I. INTRODUCTION

## A. PROBLEM STATEMENT

The U.S. Navy (USN) and Marine Corps (USMC) depend heavily on gas turbines and internal combustion engines as prime movers and as sources of energy for electricity generation. Large diesel and gas turbine engines are used to power and propel ships, aircraft, and vehicles, power shore-based installations, and power forward operating bases around the world. With the ability to deploy these assets the U.S. Navy and Marine Corps bring unmatched capabilities to the battlefield, but there are drawbacks. Two of the biggest challenges the military faces with these technologies are the military's dependence on petroleum-based fuels and masking the copious amounts of thermal radiation these high-energy engines give off.

The Secretary of the Navy (SECNAV) has made energy efficiency a priority for the USN and USMC. The "Strategy for Renewable Energy" [1] lays out the SECNAV's five energy goals. Goal #1 calls increasing the use of alternative energy use DON-wide, and Goal #2 calls for making 50% of shore activities, such as U.S. Naval base power stations, energy net-zero by 2020. The USN and USMC have previously relied on industry leaders and vendors to source the best possible energy harvesting technology, but little attention has been given to the proper placement of energy harvesting devices for optimal energy recovery and maximum reliability. In particular, waste heat recovery (WHR) devices present their own special set of challenges due to complex engine exhaust flow patterns, geometric limitations, pressure drop that negatively affects engine performance, and their harsh operating environment, often cycling between room temperature and hundreds of degrees Celsius.

In addition to WHR issues, enemies and potential enemies of the United States possess infrared detecting equipment and weapons that could allow them to locate and destroy Navy and Marine Corps high value assets. For this reason, it is imperative we continue to conduct research aimed at reducing the effective IR signature of diesel and gas turbine engines, as they will continue to be a valuable and prevalent source of energy

for the Navy and Marine Corps for the foreseeable future. To achieve this, the USN and USMC must increase their intellectual capital through studies seeking to better understand the complex temperature and velocity distributions in exhaust systems.

This study was conducted as part of the Naval Postgraduate School's (NPS) commitment to solving WHR issues for the USN and USMC. The NPS WHRS Program Roadmap shown in Figure 1 provides NPS's plan to build WHR subject matter expertise and provide solutions for issues relating to WHRS (Waste Heat Recovery Systems) reliability and performance to support the strategic goals of the SECNAV's Energy Program for power generation at shore installations, at sea, and at forward-operating bases. This study uses a non-dimensional approach to cover a wide range of WHR parameters that are applicable across a large variety of prime movers and generators.

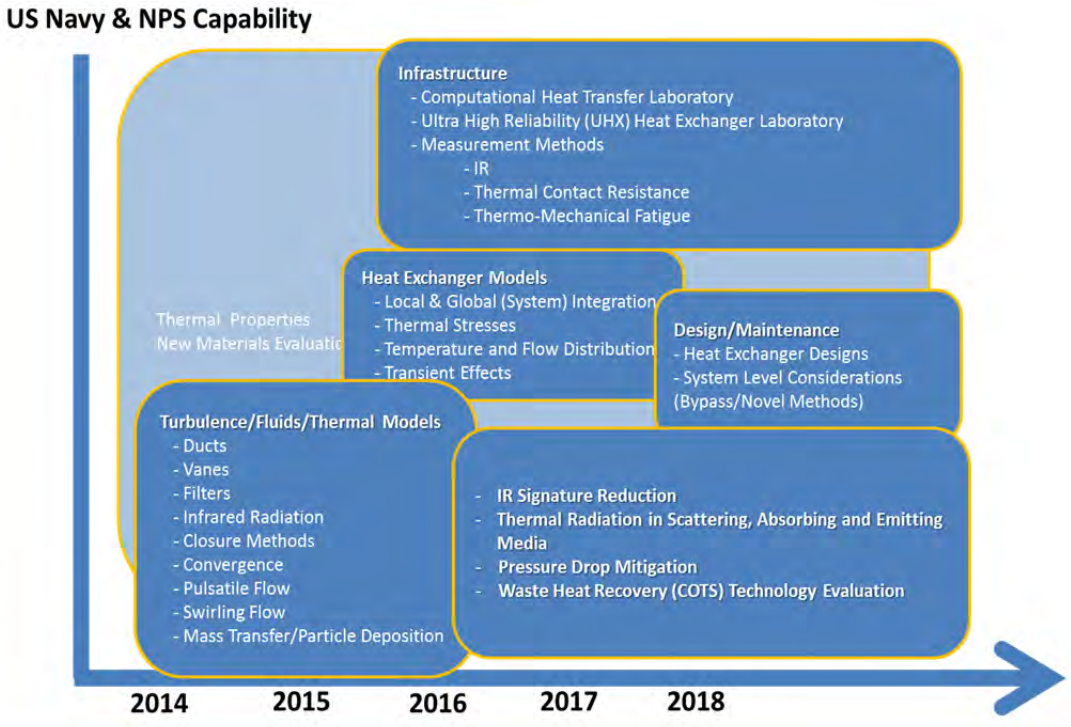


Figure 1 NPS, USN, and USMC Waste Heat Recovery Systems Roadmap, from [2]

## B. AIM

The aim of this work is to use computational fluid dynamics (CFD) software to model and predict the most optimal placement of a WHR device in an exhaust duct and secondarily determine its effect on the emitted infrared radiation from an exhaust duct. Optimal placement in this study primarily means maximizing the heat transfer to a non-intrusive WHR device, but may also mean avoiding areas with high temperature gradients to prevent adverse thermal stresses. A non-intrusive WHR device is one that does not induce a pressure drop in the exhaust system from the presence of the device. An example of such a device would be a thermoelectric generator placed on the perimeter of the exhaust ducting. A full design would also consider the effects of cost, spatial considerations, and output performance requirements.

The validation of the laminar and turbulent models in this thesis directly contributes to the NPS WHRS Team deliverables outlined in the WHRS Roadmap in Figure 1. Building organic capability through rigorous research, modeling, and testing is critical to the success of the joint effort between the NPS WHRS Team, ONR, and other key partners to solve WHRS problems and create value for the USN and DoD. The NPS WHRS team is well posed to aggressively develop the capabilities to meet its objectives and deliverables as defined by the WHRS Roadmap. This thesis builds the groundwork for accurate, efficient, and trustworthy turbulent flow heat transfer modeling for WHRS capability development and analysis.

## C. SCOPE OF REPORT

The presented work validates a 2-D model using theoretical and experimental results, and, based on geometry and flow parameters, provides a means of non-dimensionally determining the optimal location of a WHR device and predicting the exit bulk temperature from which the infrared signature can be interpreted. A 2-D model allows for simplifying assumptions that make it possible to explore a large number of "what if" scenarios while still capturing the essence of the optimization process without losing much accuracy. This simplified model reduces the complexity of the problem so the most important aspects can be analyzed with greater clarity.

## D. LITERATURE REVIEW

### 1. WHR

The USN previously employed exhaust WHR boilers aboard the Spruance class destroyers and Ticonderoga class cruisers to harvest energy from gas turbine engines; however, these systems were plagued with reliability issues as discussed by Koh [3]. One of the major issues with these systems was failure due to thermal stresses from high temperature gradients [4]. Additionally, these WHR devices were intrusive to the exhaust system and caused pressure drops that were detrimental to engine performance [3]. At the time of writing this thesis, there does not seem to be any body of research within the USN that addresses the optimal placement of WHR devices. This study of optimal placement will address both maximizing heat recovery and provide insight into addressing reliability issues with respect to adverse thermal gradients.

The USN's Electric Ships Office (PMS 320) has specifically identified development of energy recovery solutions as part of its near-term focus through 2023 in the PMS 320 "Naval Power Systems Technology Development Roadmap." PMS 320 noted that the highly transient nature and space constraints of shipboard operating environments will limit the application of commercially available WHR systems [4]. Koh [3], for example, modeled concentric counter flow WHR heat exchangers and found that heat transfer rates could be increased by offsetting the coolant fluid inlets—something that had not been done in the commercial models he researched which were being offered to the USMC. Thus, it is very important to understand the effects that constraining geometries and different flow regimes have on heat recovery and the placement of WHR devices.

Similarly, the Marine Corps Expeditionary Energy Office (E2O) hosts an annual demonstration known as Expeditionary Energy Concepts (E2C) (previously known as Experimental Forward Operating Base (ExFOB)) to bring together stakeholders from the Marine Corps and industry to demonstrate off-the-shelf technologies for future consideration and testing that may become Programs of Record [5]. At ExFOB 2014 a WHR / energy storage device was demonstrated, but one of its major drawbacks was that

it did not effectively address the importance of the WHR device placement for maximum effectiveness. Notably, there was no discussion of exhaust pressure drop and thermal stresses within the device.

A review of the literature revealed that the type of heat exchanger used influences both the effectiveness and life of a WHR device [3], [6]. Koh [3] indicated through his literature review and research that the high temperature differentials in parallel heat exchangers degrade their reliability. Large temperature gradients in dissimilar materials cause damage from differential thermal expansion and eventually lead to failure much more quickly than in counter flow heat exchangers. Typically, counter flow heat exchangers have higher heat transfer effectiveness [3], [6].

A large effort has been made to look for ways to extract waste heat energy from hot exhaust gases [3], [7], [8], [9], [10]. Koh [3] explored a great number of references in his thesis, but neither his research nor that of the any of the other authors reviewed have made reference to specific locations a WHR device should be placed to maximize heat recovery. Di Bella [7] of Concepts NREC presented a report summarizing the preliminary findings of USN funded SBIR Project # N103–229–0533. Concepts NREC, the company funded for the SBIR, analyzed the use of a thermoelectric generator (TEG) combined with a supercritical $CO_2$ (S-$CO_2$) Brayton cycle WHR device and produced a feasibility study indicating that these systems could help “provide 20% improvement in the fuel efficiency of the gas turbine propulsion engines during their projected part-load duty cycle” [11]. For an MT-30 gas turbine engine, which is used in the DDG-1000 class ship, Concepts NREC predicted a 24% improvement in power recovered when using a combination of the TEG and a supercritical $CO_2$ WHR device with 5% of the improvement coming from the use of the TEG [11]. The WHR device design by Concepts NREC does impose some pressure drop penalties in the exhaust system, but because their design incorporates a TEG, it was one of the least intrusive methods found in the literature review. After concluding this thesis, it is believed that harvesting the amount of thermal energy claimed by Concepts NREC in a high Reynolds number flow such as a gas turbine engine would be very difficult to do without imposing larger flow obstructions and inducing more pressure drop than described by Concepts NREC [7].

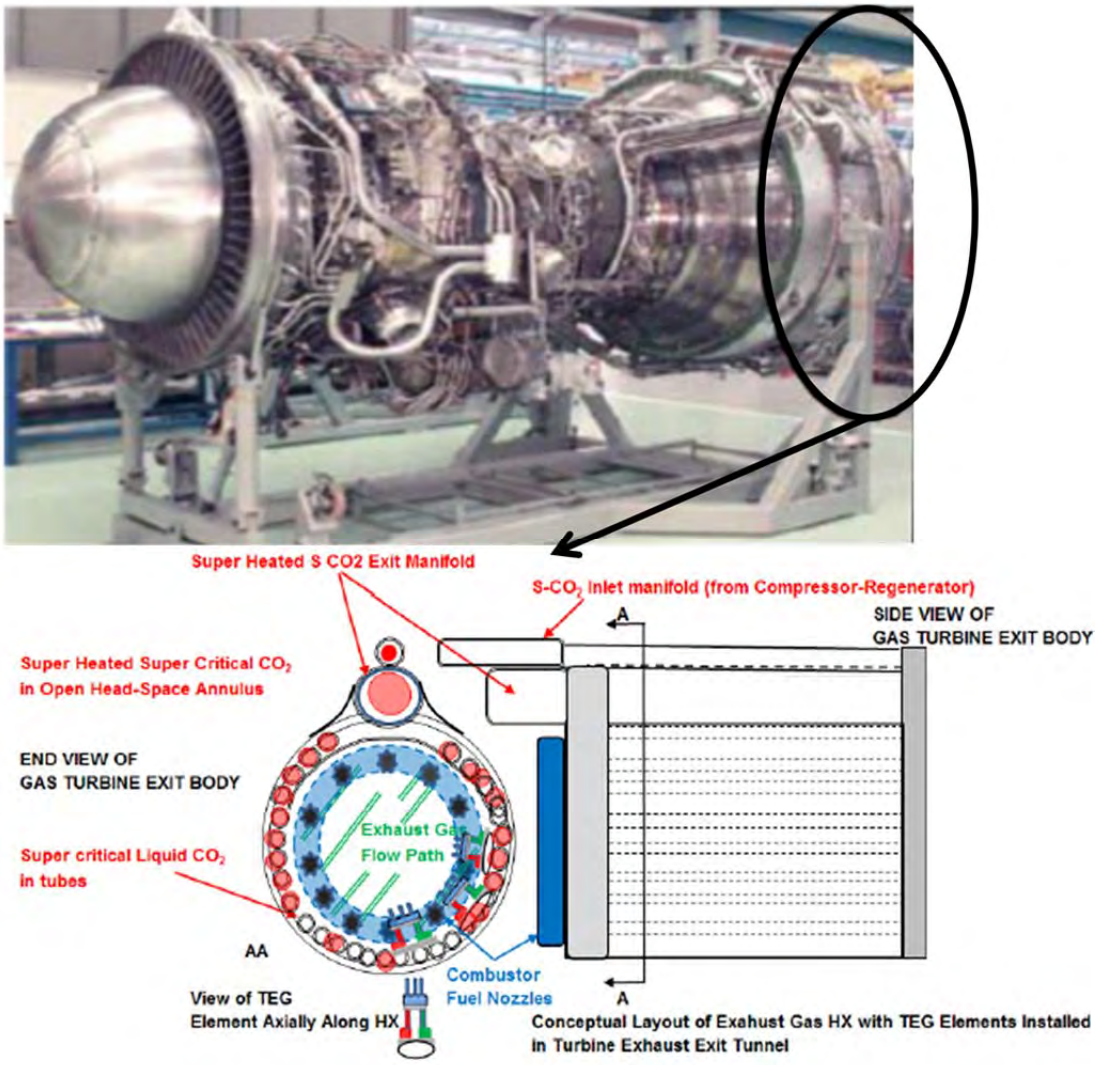


Figure 2 Conceptual schematic of the use of TEG devices installed along gas turbine tunnel—dotted lines indicate TEG elements along exhaust duct wall, from [12]

Di Bella of Concepts NREC [11] had proposed several locations for the placement of the TEG but did not justify in detail how they came to this decision other than that the temperature of the exhaust gas would be highest at these points. One schematic proposed placing the TEG along the inner and outer exhaust duct walls immediately after the power turbine (see Figure 2) [12]. The discussion of placement did not take into account the changing geometry of the exhaust duct and the characteristics of the flow such as the 90-degree bend located immediately after the exhaust inlet which is

common to USN combatant ships. TEG systems are promising because they can extract energy (albeit smaller amounts) without obstructing the flow and inducing a large pressure drop. However, the literature review did not find anything pointing out how to optimize placement of a TEG device or anything quantifying its effect on the IR signature of an exhaust plume.

## 2. IR Reduction

All objects emit radiation at all wavelengths for a given temperature, but gas turbine and diesel engines emit especially high radiation in the infrared (IR) band due to the temperature at which they operate. In fact, exhaust temperatures emit their highest amounts of radiation in the infrared zone when compared against a Planck distribution. Figure 3 shows the blackbody Planck distribution of emitting radiation in the typical operating range of engines used by the USN and USMC. As shown by Wien's displacement law the wavelength of maximum radiation intensity shifts to the left (gets smaller) with increasing temperature [6]. From Figure 3 it can be seen that the expected peak intensity of radiation is within the spectrum from 3–7 $\mu m$. Table 1 is a list of the wavelengths of peak radiation for each operating temperature. Spectral blackbody emissive power as computed in Figure 3 is defined in Incropera and DeWitt [6] as:

$$E_{\lambda,b}(\lambda,T)=\frac{C_1}{\lambda^5\left[e^{(C_2/\lambda T)}-1\right]} \tag{1}$$

$C_1=2\pi hc_0^2$=3.742 x $10^8$ $W\cdot\mu m^4/m^2$ and $C_2=hc_0/k$=1.439 x $10^4$ $\mu m\cdot K$ where h=6.6256 x 10–$^{34}$ $J\cdot s$ and k=1.3805 x 10–$^{23}$ $J/K$ are the universal Planck and Boltzmann constants, respectively, and $c_0$=2.998 x $10^8$ m/s is the speed of light in a vacuum [6].

Table 1 Wavelength of peak radiation from 400 K to 800 K

| **T (K)** | $\lambda(\mu m)$ |
|---|---|
| 400 | 7.2 |
| 500 | 5.8 |
| 600 | 4.9 |
| 700 | 4.2 |
| 800 | 3.6 |

The company FLIR (forward-looking infrared) Commerical Vision Systems B.V [13] indicates that there are two bands of particular interest for IR detection. They are the midwave IR (MWIR) band from 3–5 $\mu m$ and longwave IR (LWIR) band from 8–12 $\mu m$. IR detection systems are generally optimized to operate in one of these two bands depending on the target [13]. Enemy detection systems are likely optimized to locate IR signatures from engine exhaust in the MWIR range so the targets can easily be distinguished from the surroundings. Many have studied how to change or suppress the IR signature that emits from high temperature engine applications [14], [15], [16], [17], [18], [19]; however, none have quantified the effect of a non-intrusive WHR device on IR signature reduction.

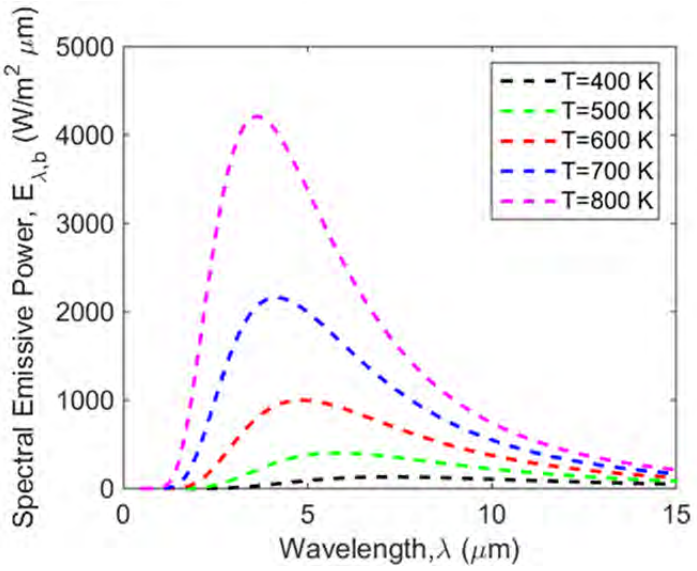


Figure 3 Spectral blackbody emissive power for operating range of typical USN and USMC engines

# II. METHODOLOGY

Engine exhausts contain extremely complex flow patterns. The flow patterns studied in this thesis are more basic representations of these complex flows yet they reveal features that would prove to be useful while making design decisions. The analysis of heat transfer and fluid flow in a 2-D 90-degree miter bend highlights the major parameters affecting WHR by removing some of the complexity without losing the essence of the problem.

The development of accurate turbulence and thermal models was very important to obtaining quality results for this thesis, and it also supports ONR and NPS WHRS Team objectives. The turbulence models validated in the thesis directly support NPS WHRS Roadmap objectives and will serve as the baseline for further research in WHRS by NPS students. Specifically this research meets the Roadmap (2014–2020) objectives aligned with building, running, and understanding thermal and turbulence models and their capabilities. This study provides first-of-its-kind insight into how to optimally place a WHR device, it adds to the body of knowledge used for studying thermal stresses in WHR devices, and it contributes in a meaningful way to NPS's knowledge base for IR signature reduction.

Beale [20] studied 2-D fluid flow over a wide range of Reynolds numbers that covered the operating ranges of the MEP-803A and the LM2500. This study will cover a similar range of Reynolds numbers, and it will also incorporate heat transfer.

## A. GOVERNING EQUATIONS

### 1. Continuity

$$\frac{\partial \rho}{\partial t} + \nabla \cdot (\rho \vec{U}) = 0 \tag{2}$$

A 2-D steady-state analysis was used as the approach for this thesis. The 2-D approach simplified the analysis and was warranted given that the largest flow gradients are in two primary dimensions. Using these simplified assumptions not only reduced the computational time but it allowed for a level of analysis that could identify subtle features

of the flow that may not have been apparent in a full 3-D analysis due to its inherent complexity. At all points continuity must be satisfied. Air as an ideal gas was the fluid analyzed in this study, so the density was variable and largely a function of temperature. In all cases, the Mach number was well below 0.3, so while changes in density were tracked, compressibility effects in terms of flow patterns were neglected.

### 2. Momentum (Navier-Stokes Equations)

$$\frac{\partial(\rho\vec{U})}{\partial t}+\nabla\cdot\left(\rho\vec{U}\otimes\vec{U}\right)=-\nabla p+\nabla\cdot\tau+\vec{S}_M \tag{3}$$

Again, because the analysis was 2-D steady-state and there are no source terms, all z terms were dropped from the Navier-Stokes equations, the first term on the left-hand side is zero, and the last term on the right-hand side (source term) is zero. Additionally, since the fluid being analyzed in all cases had a Peclet number much greater than one ($Pe \gg 1$) and the ratio of Grashof number to Reynolds number squared was much less than one ($Gr/\mathrm{Re}^2 \ll 1$), the buoyancy term was neglected. $\tau$ represents the stress tensor in the fluid. ANSYS CFX, the program used for solving the governing equations, uses time-averaged terms to model turbulent flow. The Reynolds averaged Navier-Stokes (RANS) equations account for shear forces induced by the turbulent nature of the flow.

### 3. Energy

$$\frac{\partial(\rho h)}{\partial t}-\frac{\partial p}{\partial t}+\nabla\cdot(\rho\vec{U}h)=\nabla\cdot(\mathrm{k}\,\nabla T)+\vec{U}\cdot\nabla p+\tau:\nabla\vec{U}+\vec{S}_E \tag{4}$$

where

$$\nabla\cdot(k\nabla T)=\frac{\partial}{\partial x}\left(k\frac{\partial T}{\partial x}\right)+\frac{\partial}{\partial y}\left(k\frac{\partial T}{\partial y}\right)+\frac{\partial}{\partial z}\left(k\frac{\partial T}{\partial z}\right) \tag{5}$$

The term $\vec{S}_E$ is an energy source term. No energy sources were used so this term goes to zero, and at steady-state the first two terms on the left-hand side of Equation (4) go to zero as well. The third term of Equation (4) includes the static enthalpy, h, instead of the total enthalpy because the thermal energy model in ANSYS was used instead of

the total energy model. Equation (4) is derived from the traditional total energy equation by subtracting out mechanical energy. This is suitable for low Mach number flows (Ma<0.3) such as in the current models. Despite its simplifications, Equation (4) is "useful for both liquids and gases in avoiding potential stability issues with the total energy formulation" [21]. Since this was a 2-D study the z terms were dropped. Viscous dissipation $(\tau : \nabla \vec{U})$ was included in this model.

## B. MODEL GEOMETRY AND SETUP

The generalized model geometry for this study is shown in Figure 4. The model was created in SolidWorks from the assembly of three separate parts. It consists of a backwards L-shaped fluid domain bounded on the inside of the L and outside of the L by a solid domain of thickness t which is the wall on the top and bottom of the fluid domain. This makes up what is referred to as the exhaust duct. The fluid domain is open at both ends of the L. The bottom left of the backwards L is the inlet to the exhaust duct, and the top right is the exit. ANSYS CFX was used to discretize and solve the governing equations for heat, mass, and momentum transfer in the fluid and solid domains. Appendix A outlines the setup for the model geometry and basic ANSYS meshing parameters. A mesh sensitivity analysis was carried out ensure optimum mesh size. An energy balance was conducted on each design run is summarized in Appendix B. All models had less than one percent numerical error.

The $k-\epsilon$ turbulence model was used for modeling turbulence in this thesis. The $k-\epsilon$ model is a robust implicit solver that is very common in many commercial codes. Rather than specifying a function for k and $\epsilon$, the turbulence intensity was specified. For all turbulent runs in CFX, medium turbulence intensity was specified (5%). From this, the solver determined the values of k and $\epsilon$ directly from the differential transport equations [21].

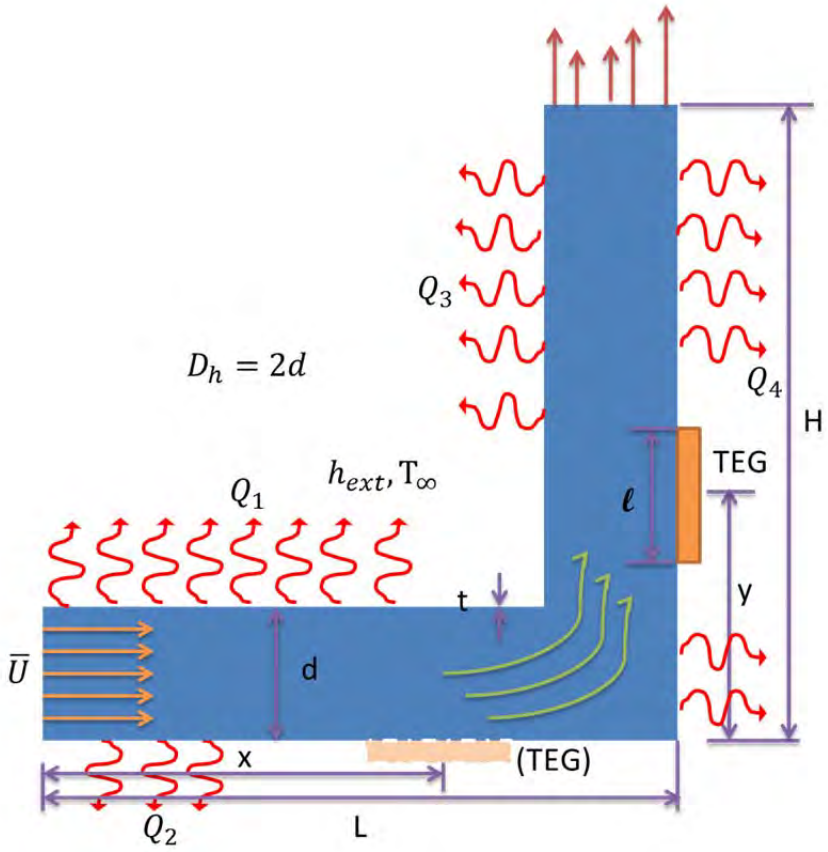


Figure 4 Illustration of dimensions used in models; $Q_1$ to $Q_4$ are the convective losses from the duct walls

Heat transfer through the walls of the duct was the primary dependent variable to be analyzed. The heat transfer at the outer wall of the duct is defined by:

$$Q = \int_0^x h_{ext}(T_w(x) - T_\infty)dx \tag{6}$$

The external heat transfer coefficient was specified for each run, and ANSYS calculated the local heat transfer coefficients inside the duct. ANSYS calculates a local near-wall heat transfer coefficient by utilizing a near-wall temperature (average of the half element temperature next to the wall node) and the wall temperature [22]:

$$h_{nw} = \frac{q"}{(T_w - T_{nw})} \tag{7}$$

This definition for near wall heat transfer coefficient is not sufficient for validating the model relationships between the bulk (mixing cup) temperature of the fluid

and the wall. In order to properly analyze the limiting cases for validation of the numerical and experimental work such as constant heat flux and constant temperature cases, the local internal heat transfer coefficient had to be defined as:

$$h_x = \frac{q''_x}{(T_{b,x} - T_w)} \tag{8}$$

The mean internal heat transfer coefficient is defined as:

$$h_m = \frac{Q}{A\Delta T_{lm}} = \frac{1}{x}\int_0^x h_x dx \tag{9}$$

$\Delta T_{lm}$ is the log-mean temperature difference defined as:

$$\Delta T_{lm} = \frac{(T_w - T_0) - (T_w - T_{b,x})}{\ln[(T_w - T_0)/(T_w - T_{b,x})]} \tag{10}$$

$T_{b,x}$ is the bulk (mixing cup) temperature of the fluid at a distance x from the entrance defined by the average enthalpy of the flow at a cross section $A_c$ :

$$T_{b,x} = \frac{\int_{A_c} c_p \rho(x,y) u(x,y) T(x,y)\, dA_c}{\int_{A_c} c_p \rho(x,y) u(x,y)\, dA_c} \tag{11}$$

For constant specific heats Equation (11) simplifies to

$$T_{b,x} = \frac{\int_{A_c} \rho(x,y) u(x,y) T(x,y)\, dA_c}{\dot{m}} \tag{12}$$

## C. NON-DIMENSIONAL VALUES AND PARAMETERS

The use of non-dimensional values and parameters was important for validating the models and for dimensionality and similitude considerations for comparison with current and future studies. A summary of the terms used follows.

$$Gz = \frac{\mathrm{D}_h}{x} \mathrm{Re}\,\mathrm{Pr} \tag{13}$$

Gz or the Graetz number is helpful in identifying non-dimensional distances in thermal-fluid applications. The inverse of the Graetz number was used quite extensively by [23], [24], and [25] in their experiments for determining the thermal entry length of simultaneously developing flows. The inverse Graetz number is denoted by x*:

$$x^* = \frac{(x / D_h)}{\mathrm{Re}\,\mathrm{Pr}} = Gz^{-1} \tag{14}$$

The Nusselt number is an important number in heat transfer. On its face, it is a ratio of convection heat transfer to diffusion heat transfer, but as Incropera and DeWitt [6] describe, it can be interpreted as a dimensionless temperature gradient at a surface of interest. The local Nusselt number at any point along the exhaust duct is defined as:

$$Nu_{x,H} = \frac{h_x D_h}{k} \tag{15}$$

The mean Nusselt number is a weighted average Nusselt number from the entry to some specified point. It is defined by a mean internal heat transfer coefficient:

$$Nu_{m,T} = \frac{h_m D_h}{k} \tag{16}$$

The subscript T denotes the case of constant temperature at the duct wall, and H is for constant heat flux. These were two of the limiting cases for validating the heat transfer in the laminar model.

The non-dimensional heat transfer parameters used in this study were found using Buckingham-Pi theorem. The following parameters were used as part of the analysis of each design parameter study.

$$Q^{**} = \frac{Q_{wall}}{\dot{m} C_p (T_0 - T_\infty)} \tag{17}$$

Q** draws comparison to the effectiveness commonly used in heat exchanger applications. It is a ratio of the heat transfer rate through the wall to the maximum possible heat transfer rate (in this case, heat loss) based on the specific heat capacity at

constant pressure and the maximum temperature difference between the exhaust gas and outside air. It could also be regarded as a form of an inverse Nusselt number, but Q** is used to highlight the relationship between Reynolds number and the ability to extract heat from the flow (see Section III.D).

Through Buckingham-Pi theorem it was found that Q** is a function of several non-dimensional variables. Figure 5 shows a visual interpretation of these variables.

$$Q^{**} = \phi(\mathrm{Re}, \mathrm{Pr}, \mathrm{L}^*, H^*, l^*, s^*, h_{ext}{}^*) \tag{18}$$

$$L^* = \frac{L}{D_h} \tag{19}$$

$$H^* = \frac{H}{D_h} \tag{20}$$

$$\zeta^* = \frac{H}{L} \tag{21}$$

$$l^* = \frac{l}{D_h} \tag{22}$$

$$h_{ext}{}^* = \frac{h_{ext}}{\dot{m} C_P / A_c} \tag{23}$$

where

$$s^*(\mathrm{x}^{**}, \mathrm{y}^{**}) \tag{24}$$

The value s* is a non-dimensional perimeter distance along the duct walls. Positive s* is associated with distance parallel to the flow from the exhaust inlet on the 90-degree bend inner walls ($Q_1$ and $Q_3$), and negative s* is measured in the same direction but is on along the bend outer walls ($Q_2$ and $Q_4$). The absolute position of s* is ultimately a function of the non-dimensional duct coordinates x** and y** as measured from the origin. The origin is at the interface of the fluid and duct wall located on the bottom left exhaust duct inlet. When referring only to the exhaust inlet x** is used, and when referring only to the exhaust outlet portion y** is used. When not used as a coordinate pair it is stated or assumed by context that x** and y** are also coincident with $Q_1$, $Q_2$, $Q_3$, or $Q_4$. They are defined as:

$$x^{**} = \frac{x}{D_h}\frac{D_h}{L} = \frac{x}{L} \tag{25}$$

$$y^{**} = \frac{y}{D_h}\frac{D_h}{L} = \frac{y}{L} \tag{26}$$

$D_h$ is the hydraulic diameter which is defined as:

$$D_h = \frac{4A_c}{P} \tag{27}$$

$A_c$ is the cross sectional area and P is the wetted perimeter.

L* is the non-dimensional length of the exhaust inlet and H* is the non-dimensional length of the exhaust exit after the 90-degree bend starting from the inner wall shared by wall $Q_2$. L and H are measured internally in the duct, not on the outside. The term l* is the non-dimensional WHR device length along the duct.

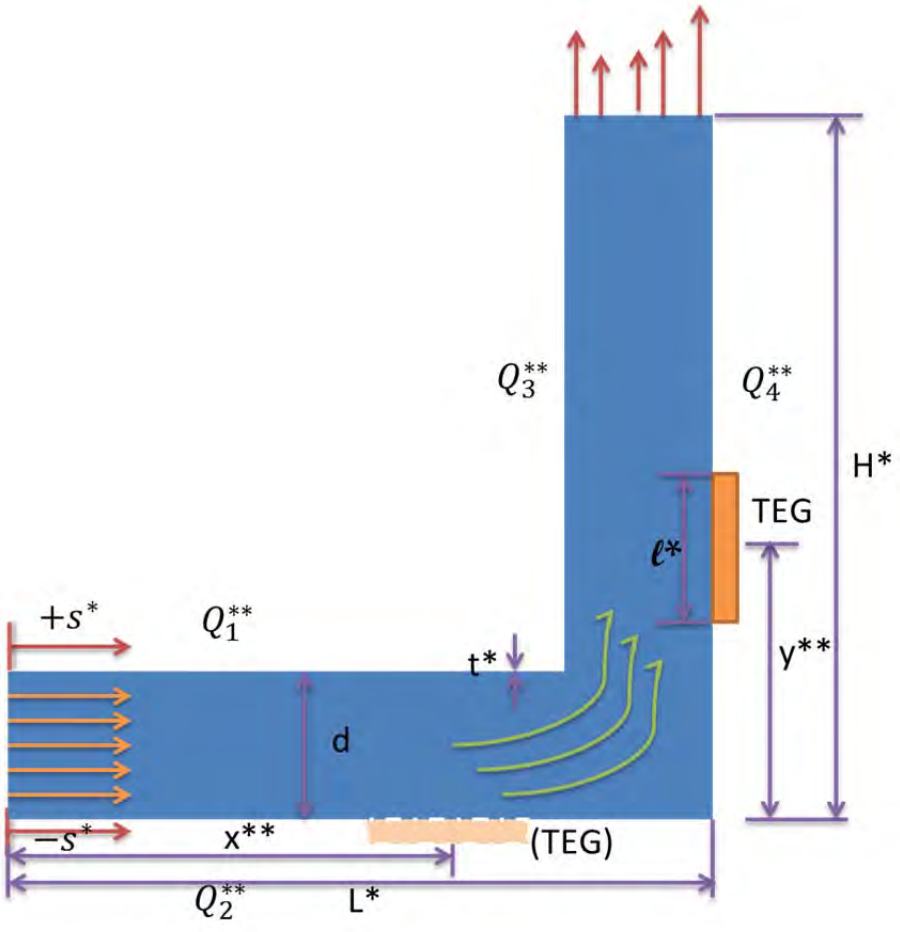


Figure 5 Illustration of non-dimensional values

Other non-dimensional values used during this thesis are non-dimensional temperature drop, heat flux, and velocity:

$$\theta = \frac{T - T_\infty}{T_0 - T_\infty} \tag{28}$$

$$\Theta = \frac{q''}{q''_{max}} \tag{29}$$

$$u^* = \frac{u}{\overline{U}} \tag{30}$$

## D. MODEL MESHING

A one division thick (2-D) sweep method with all quad face elements was used for meshing the model. After conducting a mesh refinement study, a mesh size of 0.005m was chosen for use throughout the model. This mesh size reduced numerical errors to less than 1% and also provided high levels of detail areas of high flow gradients by utilizing low aspect ratio hexahedra elements. This mesh size was used globally to simplify the parameterization process. The lengths L and H were set as geometry input parameters in ANSYS Workbench. ANSYS automatically manipulated the SolidWorks geometry, meshed, and solved for each model run. Having a consistent mesh size throughout ensured a clean, good quality quad mesh for each model run. An expression for energy balance was used as a Workbench output parameter to verify the accuracy of each run. The solver y+ at all walls was less than 11.083 for all models. ANSYS reports for the LM2500 and MEP-803A models are presented in Appendix C. All turbulent flows were solved with the $k-\epsilon$ turbulence model.

## E. LAMINAR MODEL VALIDATION

The laminar model validation was completed by comparing the CFD results with theoretical and experimental data for an extended exhaust inlet section. The exhaust inlet section was lengthened to $12D_h$ to allow for accurate assessment of the heat transfer in the straight inlet section without excessive disturbances from the 90-degree bend traveling upstream. The purpose of validating the inlet section only was to ensure that

ANSYS CFX was properly solving the mass, momentum, and energy equations for the most basic case while still keeping the bend in the model.

A constant temperature was imposed on the solid cross section of the exhaust inlet to simulate conduction from the engine heating the exhaust manifold duct walls near the connection between the two. For purposes of validation this boundary was set as adiabatic (with respect to where the exhaust manifold would connect with the engine) so direct comparison could be made with literature. This also lessened the effect of the anomalies at the beginning of the exhaust duct, which is an artifact of CFD where the program tries to simultaneously impose two temperatures at one node resulting in a singularity. This is nuance of commercial CFD code that is only recognized through experience.

In the problem being analyzed the hydrodynamic and thermal boundary layers develop simultaneously from a slug velocity and temperature inlet profile. Numerous authors have studied the problem of simultaneously developing flow between two parallel plates [23], [24], [25], [26]. Typically authors study the case of fluid heating between the plates rather than cooling or heat loss which is being studied here. There are two limiting cases that can be validated: constant heat flux and constant temperature. For the heating scenario constant heat flux and constant temperatures can be specified both in CFD simulations and in experiments. This is accomplished by using an electric heater with constant power output for constant heat flux or immersing a heated body in a large liquid domain with high heat capacity and sufficient convection or at a point of phase change to maintain the surface at constant temperature. The case of constant heat flux and constant temperature are a bit more difficult to create for a cooling case, but it can achieved in CFD software by manipulating the overall external heat transfer coefficient.

In order to simulate constant temperature for the cooling (heat loss) case, the external heat transfer coefficient is made very large. This allows the boundary temperatures to approach the ambient temperature at all points on the model. A wide range of increasing external heat transfer coefficients were tested to understand the effect, and for the purposes of this model an external heat transfer coefficient of 1000

$W/(m^2K)$ provided the necessary boundary condition while not imposing a large penalty to computational time.

The opposite scheme was carried out to simulate constant heat flux. A very low external heat transfer coefficient produced satisfactory conditions for constant heat flux, and a value of 0.001 $W/(m^2K)$ was used for the current validation.

### 1. Combined Entry Length: Constant Temperature Case

The combined entry length laminar model was validated using the results of Hwang and Fan [25], which were determined to be the most accurate results from Shah and Bhatti [24].

Stephan [26] obtained an approximate series solution for the constant temperature case of simultaneously developing flow. As indicated in Shah and London [23], Stephan's empirical equation is valid for predicting the mean Nusselt number for a Pr range of 0.1 to 1000:

$$Nu_{m,T} = 7.55 + \frac{0.024(x^*)^{(-1.14)}}{1 + 0.0358(x^*)^{(-0.64)} Pr^{(0.17)}} \tag{31}$$

Figure 6 compares the laminar model against Stephan's solution. The $Nu_{m,T}$ values are plotted against the non-dimensional duct length x*, which is the inverse of the Graetz number. Stephan's solution [26] shows good correlation with Hwang and Fan's all numerical solution [25] as indicated by both Shah and London [23] and Shah and Bhatti [24]. The current model shows good agreement with Stephan's correlation [26] and is now validated for the constant temperature combined entry case. Note that the model includes the downstream 90-degree bend. Constant temperature was simulated using $h_{ext}$=1000 W/m$^2$K, $k_{wall}$=5000 W/mK.

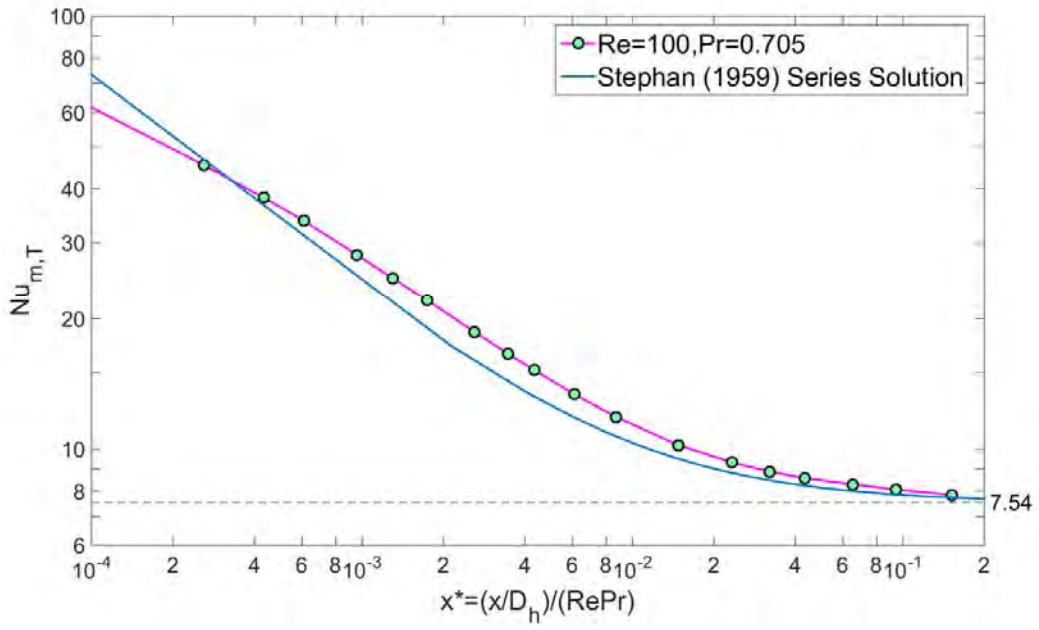


Figure 6 Parallel plates: mean Nusselt number as a function of x* for simultaneously developing laminar flow along inlet section

## 2. Combined Entry Length: Constant Heat Flux Case

The laminar model values for the constant heat flux case were compared directly with Hwang and Fan's solution [25] as plotted in Shah and London [23]. In Figure 7 the local value $Nu_{x,H}$ is plotted against x* and shows excellent agreement with Hwang and Fan's solution. Note again that the model includes the downstream 90-degree bend. Constant heat flux was simulated using $h_{ext}$=0.001 W/m$^2$K, $k_{wall}$=0.1 W/mK. Thus, the entrance portion of the laminar model is also validated for the constant heat flux case, and it can be assumed that the heat transfer is being modeled accurately.

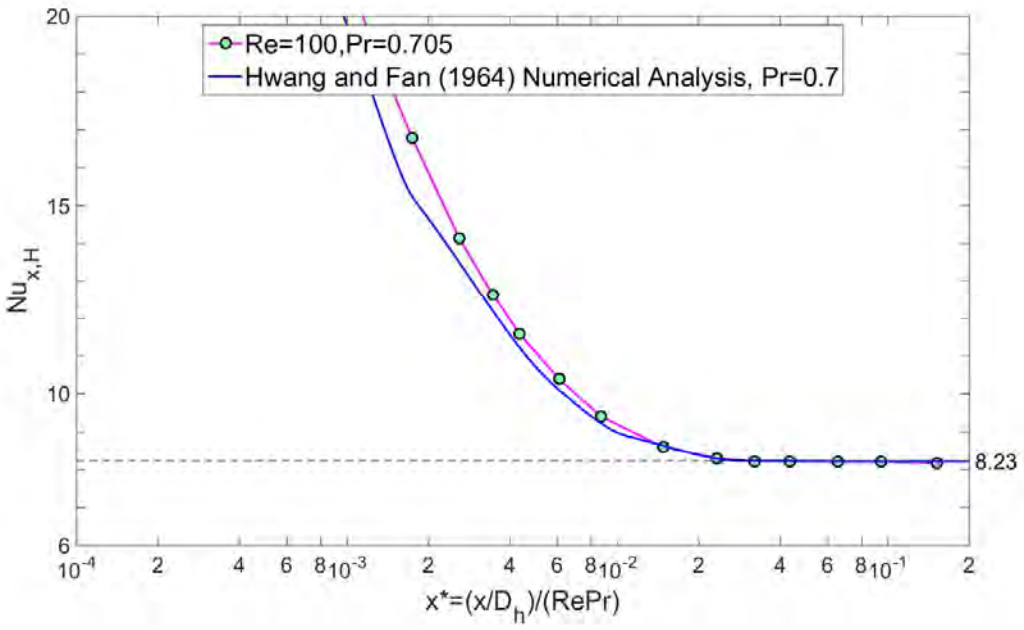


Figure 7 Parallel plates: local Nusselt number as a function of x* for simultaneously developing laminar flow along inlet section

## F. TURBULENT MODEL VALIDATION

Accurate turbulence model development supports achievement of ONR and NPS WHRS Team objectives as illustrated in the fiscal year 2015 and 2016 WHRS Roadmap (see Figure 1). Validation of the $k-\epsilon$ models for the various exhaust duct configurations used in this thesis builds the intellectual capital of the NPS WHRS Team and provides a solid base for continued growth of corporate knowledge within the ranks of NPS faculty and Naval officers who will go on to one day become program managers for major ACAT I and II level acquisition programs within the USN and DoD.

The turbulent model validation required rigorous literature research and in-depth knowledge of ANSYS CFX post-processing software. The body of research exploring turbulent flow heat transfer in 90-degree miter bends between flat parallel plates is sparse at best. However, it is a critical area of study because it represents a very common geometry encountered in flows with WHR applications. Although the geometry is simple, the flow and heat transfer through it is quite complex and still not fully understood. Growing the body of knowledge on this simple case lends advantage to studying more

complex 3-D geometries, and it provides useful insight into the major factors affecting fluid flow and heat transfer in WHR applications.

Joshi and Shah [27] provide an overview of heat transfer in a wide range of bends and fittings but only make a cursory reference to heat transfer in 90-degree miter bends with rectangular cross sections. Joshi and Shah [27] do make reference to Tailby and Staddon's [28] work in 90-degree pipe bends, where they point out an increase in peak Nusselt number in the bend outer wall as compared to the straight pipe case. For a 90-degree miter bend pipe Tailby and Staddon [28] point out that the peak Nusselt number at the bend outer wall (referred to as walls $Q_2$ and $Q_4$ in this thesis) is twice that of the straight pipe, but they do not provide the location of the peak Nusselt number. Tailby and Staddon only analyze the Nusselt numbers within the 90-degree bend and do not study the effects downstream of the bend. Yamashita et al. [29] studied heat transfer in a 90-degree miter bend between two parallel flat plates and indicated the location of peak local Nusselt numbers including those downstream of the bend; however, their work lacks a thorough explanation for the increased heat transfer rates on the bend inner wall (see Section III.B.2). The work by Yamashita et al. shows a peak Nusselt number on the bend inner wall downstream of the bend that is approximately the same magnitude as the peak Nusselt number on the bend outer wall. While Yamashita et al. [29] relate the increased heat transfer to the main flow impingement, thin thermal boundary layer, and large turbulent energy (see Figure 8), there is a need to visualize the flow in these areas to better understand the mechanism. This is especially important because none of the above mentioned authors give results for a discrete WHR device of variable length. The experimental results of Yamashita et al. [29] are compared to the models in this thesis for validation purposes.

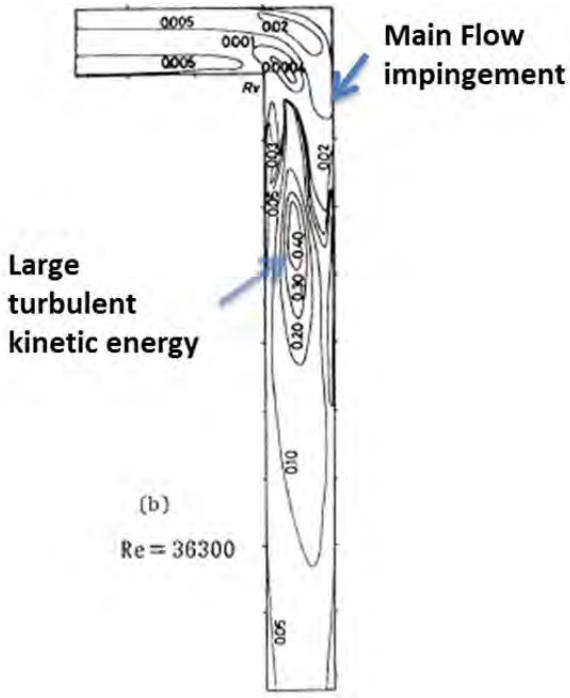


Figure 8 Contour of $k/(1/2)\,u_m^2$ (intensity of velocity fluctuation) from Yamashita et al. [29]

### 1. Velocity Profiles through 90-Degree Bend

The use of ANSYS Workbench parameter sets made analysis of various geometric and flow configurations extremely easy to conduct in rapid succession (see Appendix A). By setting Reynolds number, H*, L*, and external heat transfer coefficient as ANSYS Workbench input parameters, the model could be configured quickly to test its validity against experimental results of similar configurations. Yamashita et al. [29] provided experimentally measured velocity profiles at various locations in a 90-degree miter bend between parallel plates (see Figure 11). Yamashita et al. took their measurements using hot-wire anemometers. Figure 9 and Figure 10 are the velocity profiles of the $k-\epsilon$ turbulence model created in ANSYS CFX. Figure 9 depicts the velocity profiles for the inlet section of the exhaust model denoted by the length L, or non-dimensionally L*. Figure 10 shows the velocity profiles after the flow turns through the 90-degree bend and enters the outlet section of the exhaust model. The heat source in the experiment of Yamashita et al. [29] was located 5d upstream from the corner of the inner bend.

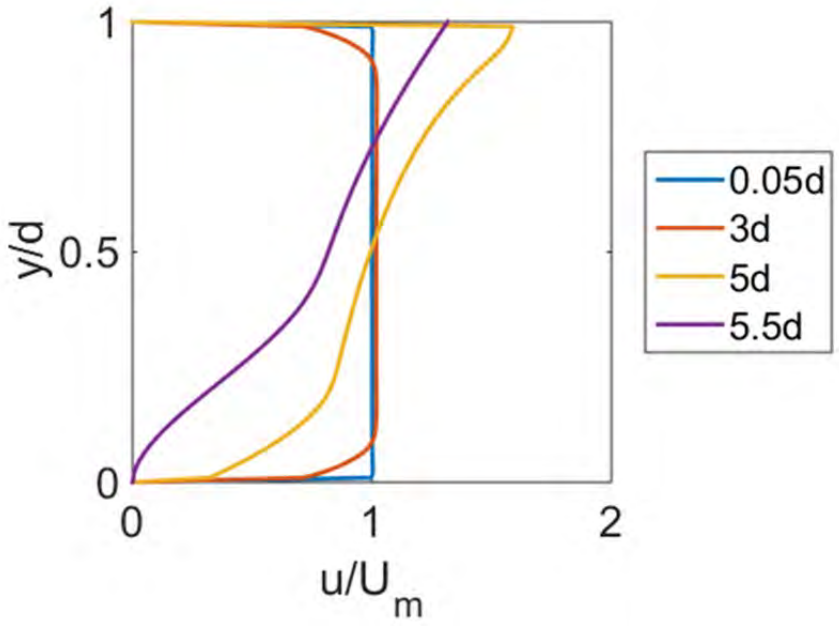


Figure 9 Velocity profiles along exhaust inlet; $h_{ext}$=5 W/m$^2$K ($h_{ext}$*=2.35 x 10–$^2$), L*=3 (H*=8), Re=36,300

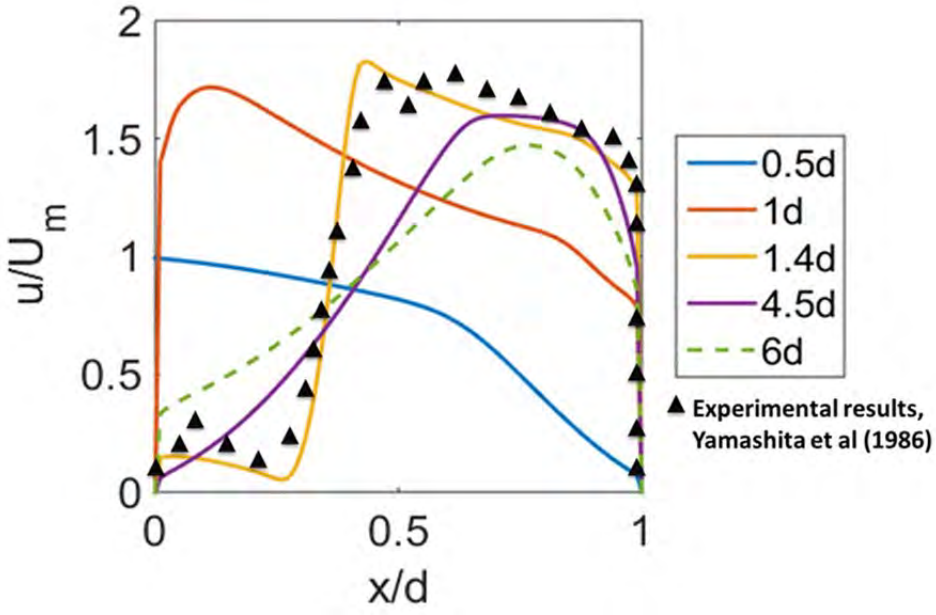


Figure 10 Velocity profiles along exhaust outlet with Yamashita et al. [29] experimental results overlaid at 1.4d; $h_{ext}$ =5 W/m$^2$K ($h_{ext}$ *=2.35 x 10–$^2$), H*=8 (L*=3), Re=36,300

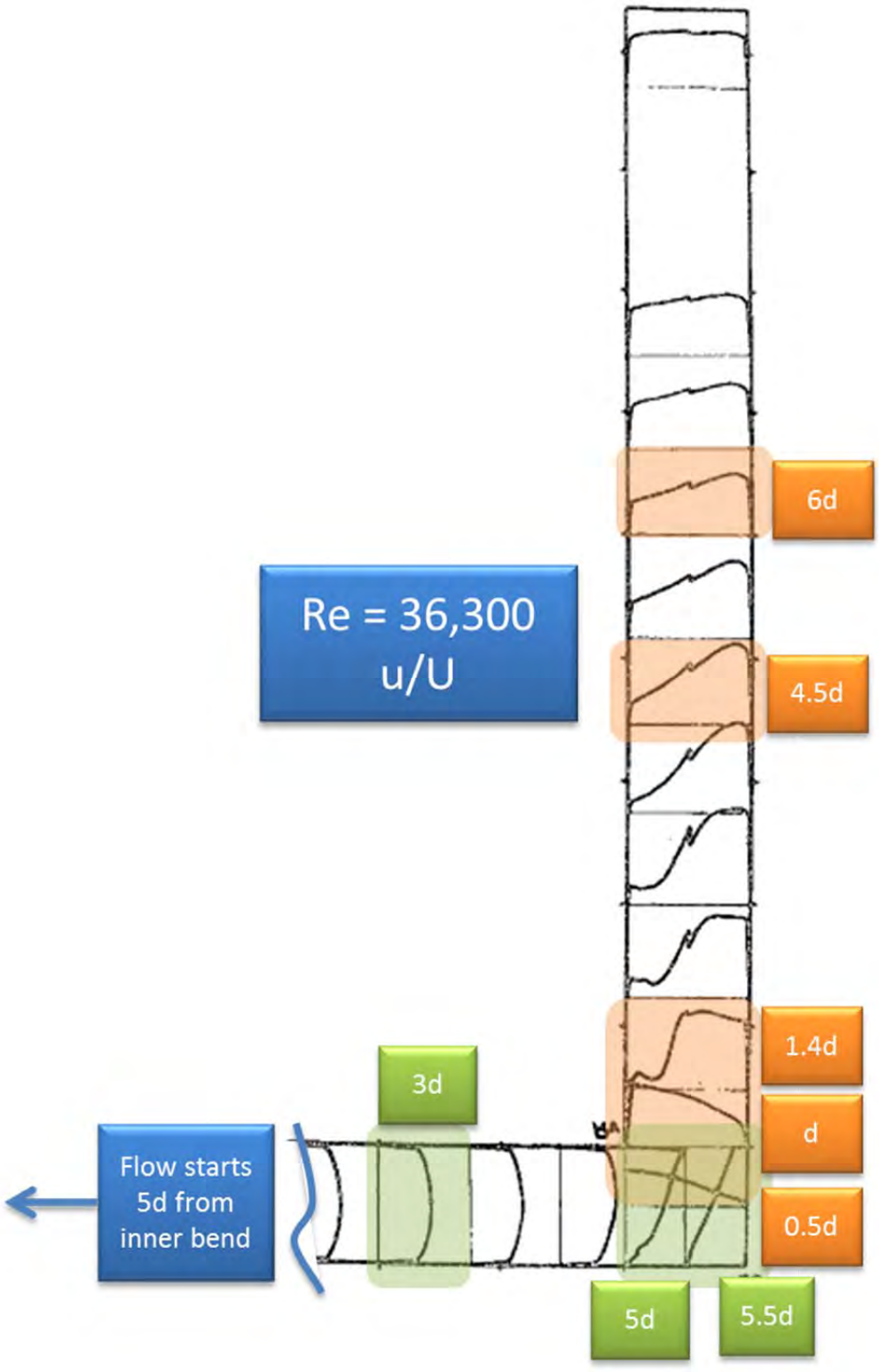


Figure 11 Velocity profiles as measured by Yamashita et al., after [29]

The turbulent velocity profiles show excellent correlation with experimental results of Yamashita et al. [29]. Most notably, the complex velocity profile at 1.4d (yellow line in Figure 10) as measured from the base of the outlet section (bend outer corner) is nearly an exact much with the experimental results in Figure 11. Results from [29] are overlaid (▲). This is the only measured velocity profile with two local maxima, and the level of correlation for this complex flow is incredible!

### 2. Change in Local Nusselt Number through 90-Degree Bend

Yamashita et al. [29] experimentally determined local Nusselt numbers were used to validate the heat transfer portion of the model. Yamashita et al. also performed a numerical analysis using a finite difference method. Error between their analytical and experimental values was attributed to inadequate parts of the turbulence model for high Reynolds number and the need for advanced techniques such as large-eddy-simulation. It should be noted that the results of Yamashita et al. [29] are for heating, while the present work concerns cooling of the flow (energy recovery). Joshi and Shah's [27] comparison of heating versus cooling in 90-degree pipe bends indicates that the peak Nusselt numbers in the heating case should be slightly higher than the cooling case. Table 2 displays the results. Joshi and Shah [27] used a correlation for heating in a helical coil since there was no correlation available for 90-degree bend heating. The correlation is attributed to Schmidt [30] and is valid for $2 \times 10^4 < Re < 1.5 \times 10^5$ and $5 < R/a < 84$ where R is the bend radius and $a$ is the pipe radius:

$$\frac{Nu_c}{Nu_s} = 1.0 + 3.6\left[1 - \left(\frac{a}{R}\right)\right]\left(\frac{a}{R}\right)^{0.8} \tag{32}$$

Table 2 Ratio of peak Nusselt numbers at the bend outer wall to Nusselt numbers for a straight pipe for turbulent flow air cooling through 90-degree bend AND helical coil heating correlation applied to 90-degree bend geometry, after [27] and [28]

| R/a<br>(Bend radius/pipe radius) | $Nu_{peak}/Nu_s$<br>*Cooling* [28] | $Nu_c/Nu_s$<br>*Heating* [27] |
|---|---|---|
| Miter bend | 2.0 | - |
| 2.5 | 1.42 | - |
| 4.0 | 1.36 | - |
| 6.0 | 1.29 | 1.71 (1.59) |
| 14.0 | 1.22 | 1.40 (1.25) |

Though Joshi and Shah [27] specified they used Equation (32), the values they presented did not match the correlation. Their values are presented in parentheses in Table 2. Nevertheless, the results still indicate that peak Nusselt numbers are smaller for cooling than heating in a 90-degree bend.

The conclusion from Table 2 supports the turbulent model heat transfer validation displayed in Figure 12 and Figure 13. Figure 12 and Figure 13 show the Yamashita et al. [29] measurements of local Nusselt number along the 2-D duct inner walls and outer walls, respectively. The inner walls are walls $Q_1$ and $Q_3$, and the outer walls are walls $Q_2$ and $Q_4$. The solid lines represent their analytical result. In Yamashita et al., H is the channel width (d in this thesis), and they used the inner corner of the 90-degree bend as the origin with positive x being parallel to the duct wall. The current turbulence model Nusselt number values are overlaid in blue plus signs and red diamonds. Again, note that the Yamashita et al. setup [29] was for heating with constant heat flux, but the turbulent model being validated is setup for cooling to model heat recovery. Although this model is for cooling, constant heat flux was simulated by making the overall external heat transfer coefficient at the walls very small so that the resulting Nusselt numbers would be similar. As seen in Figure 12 and Figure 13, the current turbulence model shows very good qualitative correlation. As mentioned previously, Yamashita et al. attributed their

numerical error (solid lines show their numerical results in the figures) to inadequate turbulence models, but given the robustness of the current ANSYS CFX $k-\epsilon$ turbulence model, it is probably more accurate to attribute the difference in values in this case to the fact that peak Nusselt numbers for cooling are lower than for heating as indicated by Joshi and Shah [27]. This clearly shows the turbulence model being used is valid for predicting heat transfer for heat recovery applications.

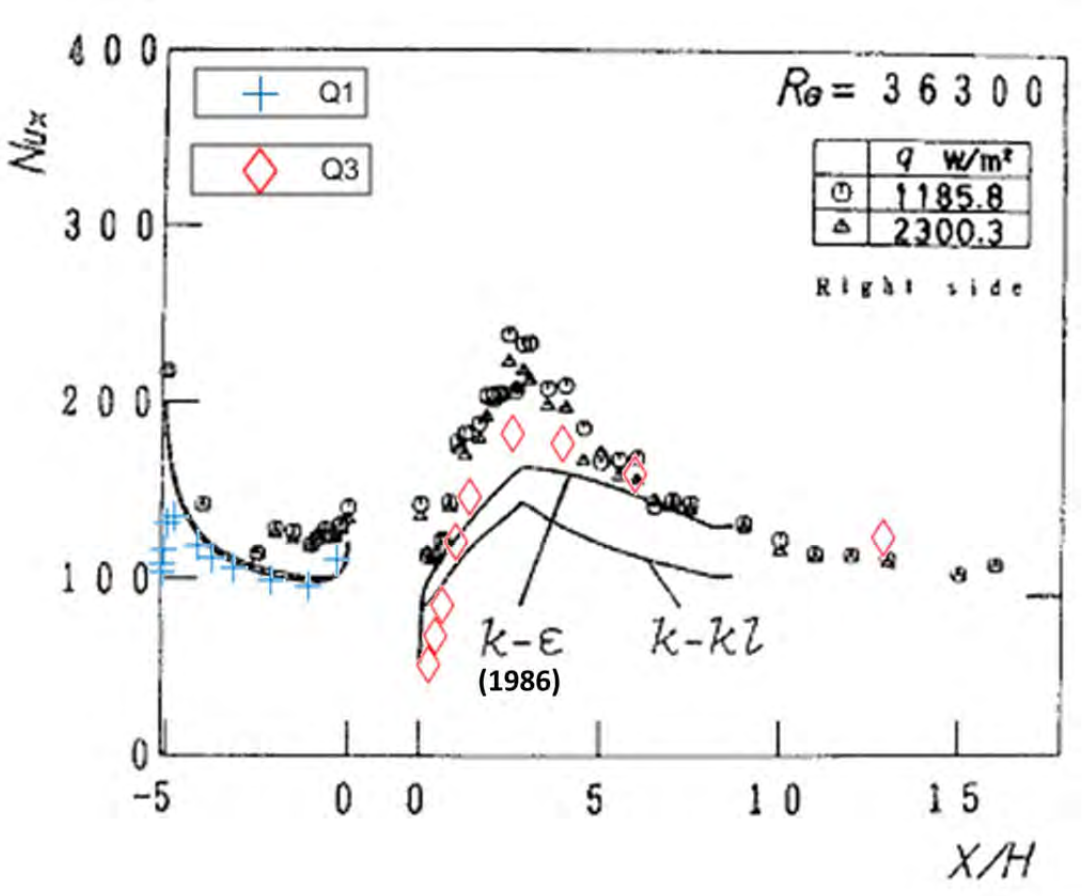


Figure 12 Nusselt number along inner walls ($Q_1$ and $Q_3$): Validation of results of local Nusselt number through 90-degree bend laid over the experimental results of Yamashita et al., after [29]

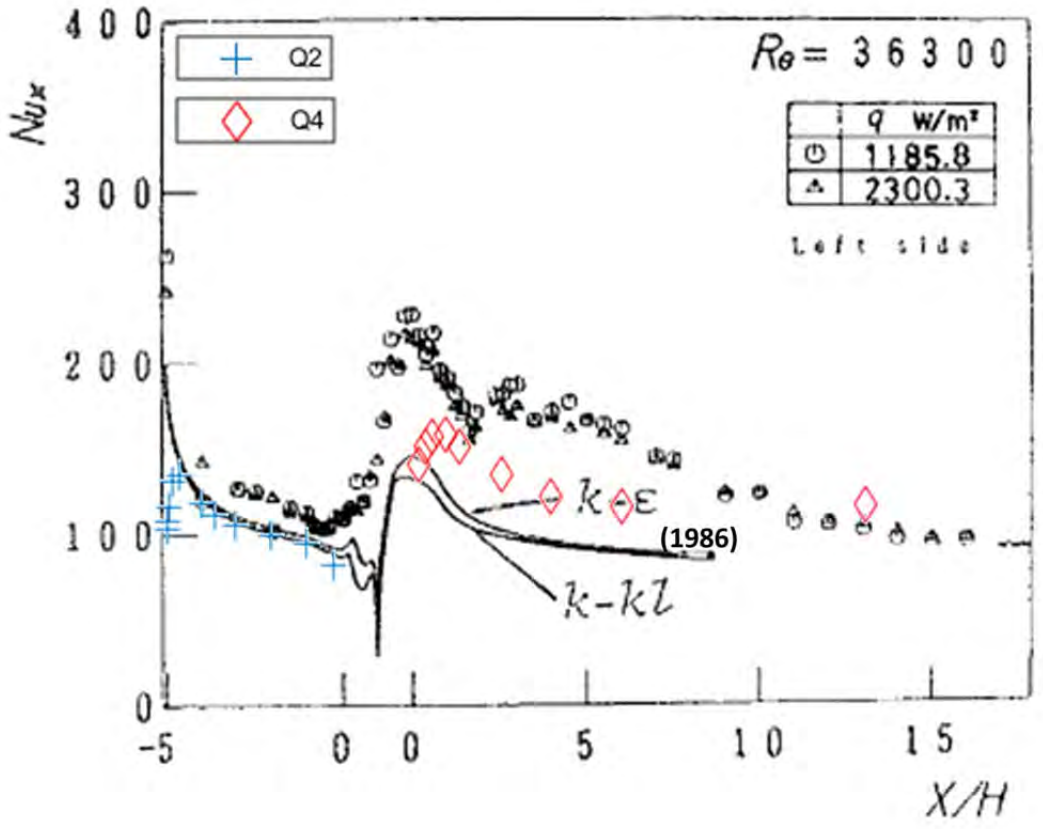


Figure 13 Nusselt number along outer walls ($Q_2$ and $Q_4$): Validation of results of local Nusselt number through 90-degree bend laid over laid over the experimental results of Yamashita et al., after [29]

THIS PAGE INTENTIONALLY LEFT BLANK

# III. RESULTS

## A. SUMMARY OF RESULTS

The results show that the Reynolds number of the flow and placement and size of the WHR device have significant effect on the recoverable heat. Local Reynolds number depression in the secondary recirculation zone enhances heat transfer, and device placement is the dominant factor for maximizing heat transfer in a given configuration; however, there are large temperature gradients present that could lead to failure from thermal stresses. Higher Reynolds number flows exhibit more sensitivity to changes in external heat transfer coefficient than lower Reynolds number flows. In all cases, changes in the geometric parameters L* and H* influence the best relative position for the WHR device. Lastly, non-intrusive WHR devices have very limited effectiveness on IR reduction.

## B. EFFECT OF WHR DEVICE SIZE AND PLACEMENT ON HEAT TRANSFER RATE THROUGH DEVICE

WHR device size and placement had a significant effect on the heat recovered from the exhaust duct. Obviously a larger WHR device will extract more energy in most cases, but there are particular areas of the duct where increasing the size of the WHR device does no more to increase heat transfer rates than moving the device to a new location. Heat recovery dependence on WHR device placement was a function of the Reynolds number and the length of the inlet and exit regions of the exhaust duct.

### 1. Device Placement

The 90-degree bend in the duct configuration studied manipulates the flow such that recirculation zones are created. In some cases, these recirculation zones create “dead zones” where heat transfer through the duct walls is severely restricted. In this case, these dead zones are the least desirable areas to install a WHR device. However, in some cases, it was found that the recirculation zones actually enhanced heat transfer. Beale [20], whose work did not consider heat transfer, found that two recirculation zones exist for the 90-degree bend geometry. A large primary recirculation zone forms in the corner of the

duct, and a secondary recirculation zone forms on the inner wall just past the bend. These two recirculation zones are shown in Figure 14. Flow separation and stagnating flow reduces the heat transfer in the primary recirculation zone, but the secondary recirculation zone actually enhances heat transfer near its top where the hot flow impinges on wall $Q_3$ and then slows down dramatically, with u*, the non-dimensional velocity, decreasing from a value of two to nearly zero. A portion of the main flow impinges on the inner wall, and this creates a local depression in Reynolds number allowing more time for heat transfer to occur where the thermal boundary layers are thinner. As the flow slows in the region along the wall the heat transfer rate increases quite significantly as illustrated in both Figure 15 and Figure 16.

Figure 15 and Figure 16 show the non-dimensional heat transfer rates for a nominally sized WHR device length (l*=0.25) at all positions on the outside of the exhaust duct. The heat transfer was measured by essentially placing the WHR device flush with the bend inner wall adjacent to the exhaust inlet and sliding it along the inner walls ($Q_1$ and $Q_3$); then starting over at the exhaust inlet again and switching sides, sliding the device along the bend outer walls ($Q_2$ and $Q_4$). The distances x** and y** are measured to the centroid of the WHR device from the exhaust inlet and bottom of the inside inlet section of the duct, respectively. The distance to the WHR device centroid is measured by x** when the WHR device is on wall $Q_1$ or $Q_2$ and by y** when it is on wall $Q_3$ or $Q_4$.

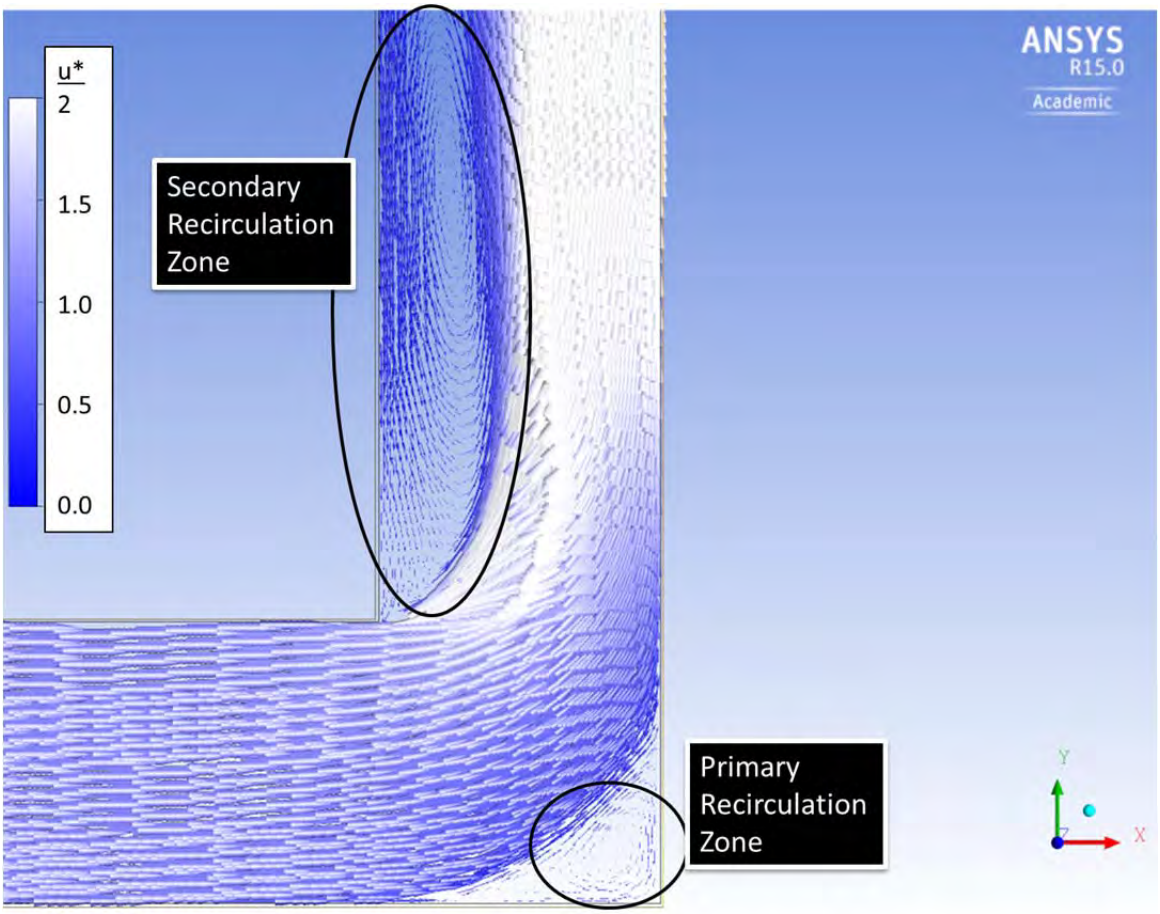


Figure 14 Primary and secondary recirculation zones near 90-degree bend

Non-dimensional heat transfer rates for the model representative of the MEP-803A dimensions and flow characteristics are depicted in Figure 15. A WHR device installed on wall $Q_1$ or $Q_2$ will recover the maximum energy when placed as close to the exhaust inlet as possible where the thermal boundary layers are still developing. Q** for wall $Q_2$ drops off as x** approaches the primary recirculation zone; x** equal to 1 is the corner of the duct at the 90-degree bend. If one were to place a WHR device after the 90-degree bend on the vertical portion of the duct, it would make more sense to place the WHR device on wall $Q_3$ near the top of the secondary recirculation zone. If space near that area was restricted then wall $Q_4$ after the primary recirculation zone would be the best placement. Q** for wall $Q_3$ stays lower than on wall $Q_4$ for the majority length of the wall due to the effects of the secondary recirculation zone. The height of the exhaust exit,

H*, in the MEP-803 is only 1.5 times the hydraulic diameter of the duct ($\zeta^* = 3/8$). The secondary recirculation zone, as seen in Figure 17, covers the entire portion of the wall $Q_3$ and even continues beyond the bounds of the duct which negatively affects the heat transfer on wall $Q_3$. Q** on wall $Q_4$ is maximum near where the flow impinges on the outside wall, $Q_4$. The amount of energy recovered on the vertical wall is very dependent on the H* dimensionless variable. Figure 15 highlights the effect of this parameter.

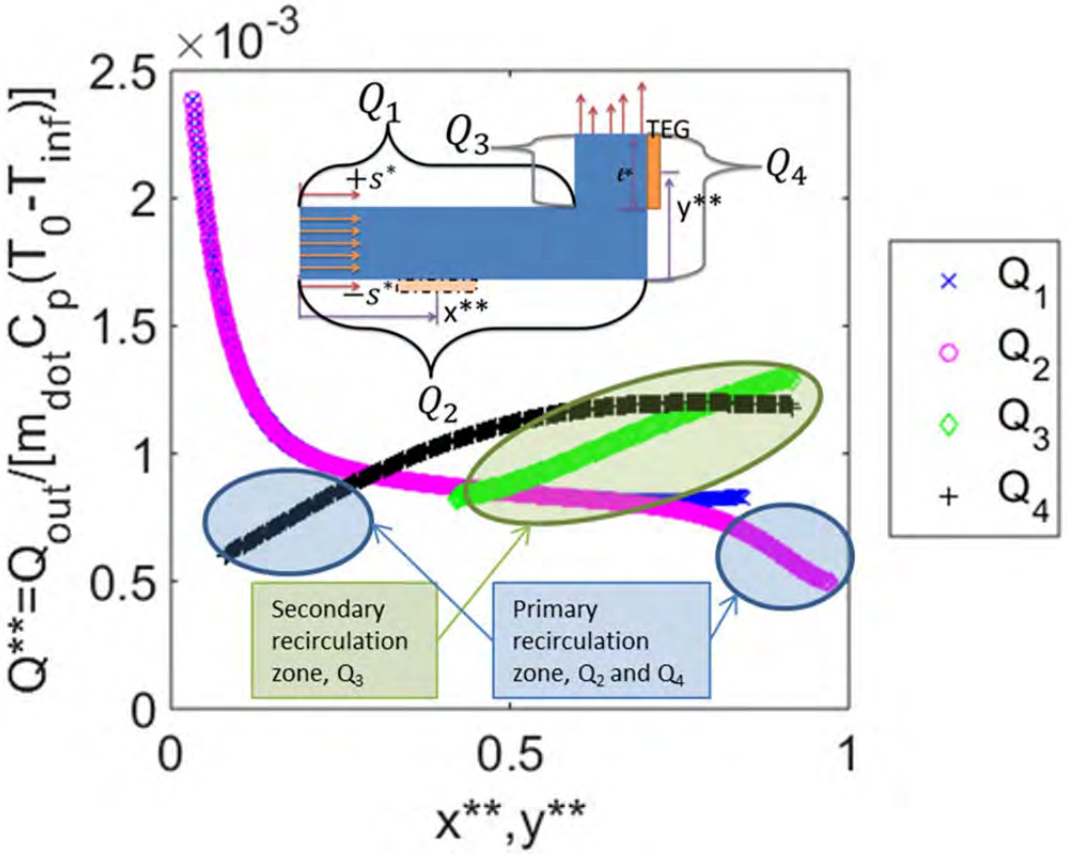


Figure 15 Effect of WHR device placement (x**, y**) on Q** for $h_{ext}$=5 W/m$^2$K W/m$^2$K ($h_{ext}$*=4.27 x 10–$^2$), L*=4, H*=1.5, l*=0.25, Re=20,000 (MEP-803A)

Figure 16 indicates the uniqueness of the flow patterns inside the walls of an exhaust duct representative of the dimensions of a shipboard LM2500 system. For this case L* is much shorter than H* ($\zeta^* = 16/3$). Notice that while walls $Q_1$ and $Q_2$ near the exhaust inlet exhibit the highest heat transfer rate, it drops off very quickly with

increasing x**. This means that only a very small portion of the exhaust inlet provides an adequate area for efficient heat transfer. For shipboard setups, the exhaust inlet region is often a difficult region to place a WHR device due to the close proximity to existing equipment such as bleed air ducts and the main reduction gear (MRG). As such, wall $Q_3$ is the best choice for WHR device placement. This is not immediately obvious and seems counterintuitive because of the location of the secondary recirculation zone, but the local Reynolds number depression in the vicinity of the 90-degree bend actually significantly increases the heat transfer through wall $Q_3$.

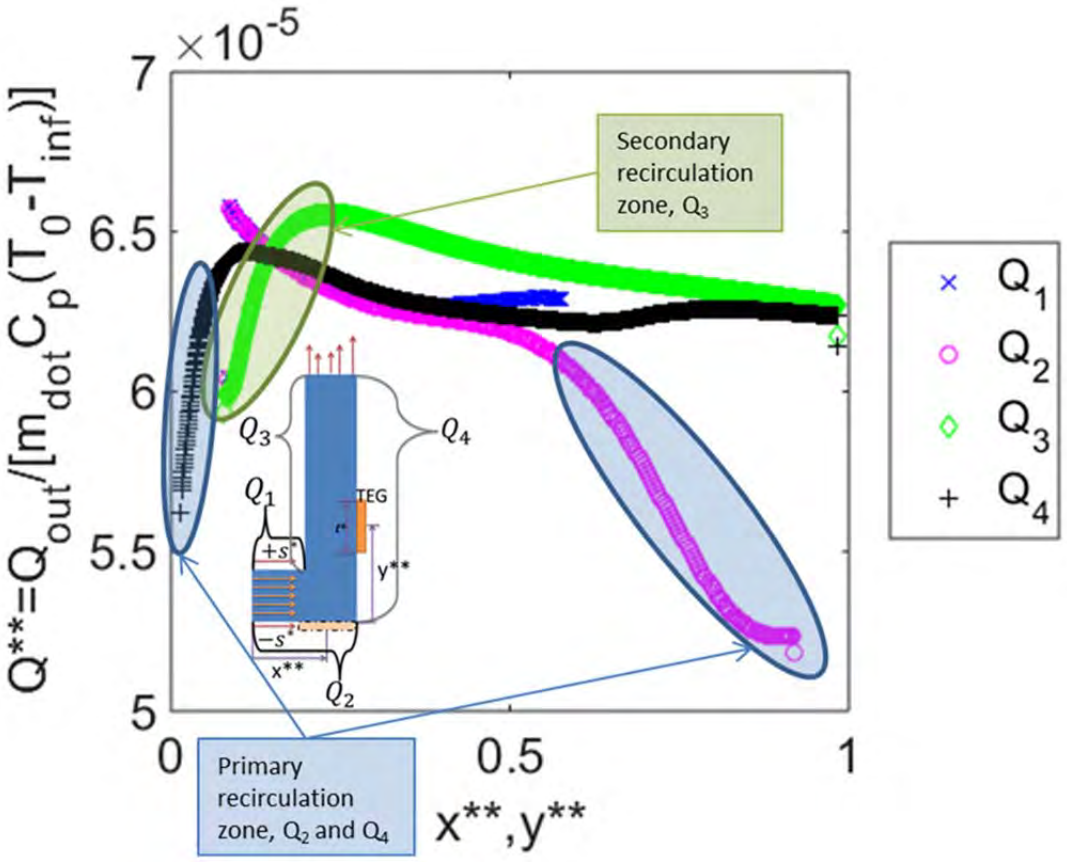


Figure 16 Effect of WHR device placement (x**, y**) on Q** for $h_{ext}$=5 W/m$^2$K ($h_{ext}$*=8.54 x 10–$^4$), L*=1.5, H*=8, l*=0.25, Re=1,000,000 (LM2500)

It is interesting to note the stark differences between the areas of maximum heat transfer between the MEP-803A model and the LM2500 model. Figure 16, which shows

the LM2500, has an H* value that is eight times the hydraulic diameter and an L* value that is only 1.5 times the hydraulic diameter ($\zeta^* = 16/3$). The secondary recirculation zone is fully enclosed within the exhaust duct for the LM2500 model. In addition, the Reynolds number is two orders of magnitude larger than the MEP-803A model in Figure 15. The higher Reynolds number accounts for lower values of Q** because the ratio of heat conducted through the walls to heat convected through the duct is much smaller, but the combination of both higher Reynolds number and varying duct geometry changes the flow pattern, and thus heat transfer, significantly (see Figure 18 and Figure 19 for dimensional heat transfer values for the MEP-803A model and LM2500 model, respectively). Unlike the MEP-803A model, the majority of wall $Q_4$ and even wall $Q_1$ are not the most advantageous places to install a WHR device. It turns out that wall $Q_3$ is best position for the WHR device for all sizes of WHR devices tested. Figure 21 shows the flow pattern in the LM2500 model, which indicates why the heat transfer rate is highest on wall $Q_3$. Again, this is counterintuitive because conventional wisdom would tell a designer to avoid areas of recirculation thinking that they would all act as "dead zones" like the primary recirculation zone. Knowing that the impinging flow and local Reynolds number depressions can improve heat transfer in flows, the flow could be manipulated to increase heat transfer in a more advantageous position on the duct through the use of turning vanes or baffles. There are important implications to this finding. Given the fact that there is currently an effort underway to increase the efficiency of the USN and USMC's prime movers and generator sets through WHR technologies, it is very important to understand that geometry and flow characteristics have a large effect on the optimal placement of a WHR device.

At low Reynolds number (~$10^4$) with small $\zeta^*$, heat recovery is maximized by placing a WHR device as close to the exhaust inlet as possible. Near the exhaust inlet a nominally-sized device can recover 75% more energy than the next best option on another wall. In contrast, for high Reynolds number flows (~$10^6$), especially with large $\zeta^*$, wall $Q_3$ reaches the same level of heat recovery as the region very close to the inlet, but it is better overall for heat recovery because the heat transfer rate is higher over a majority of its length and does not decay quickly like it does near the inlet region. Also of

note, centering a WHR device on wall $Q_3$ only two hydraulic diameters above the bend inner wall increases the heat recovery in the high Reynolds number case (~$10^6$) by 10% compared to placing the device near the corner of the 90-degree bend, or there is a 25% increase in heat recovery compared to placing the WHR device at the primary recirculation zone on the bend outer wall on wall $Q_2$. Take note, though, of the steep temperature gradients in these regions, which mean that the thermal stresses could be high. Seeking out the peak heat recovery rate may not always be the most viable option when considering wear and tear on equipment. Even though wall $Q_4$ has a lower heat transfer rate than $Q_3$, the heat flux gradient, and therefore temperature gradient, is smaller. This may be more desirable for a sensitive piece of equipment or WHR device. This makes wall selection very important. If a WHR device is only arbitrarily placed, it may not achieve the maximum efficiency possible; or worse, it could fail due to thermal stress loading and may not justify the costs associated with installing such expensive equipment.

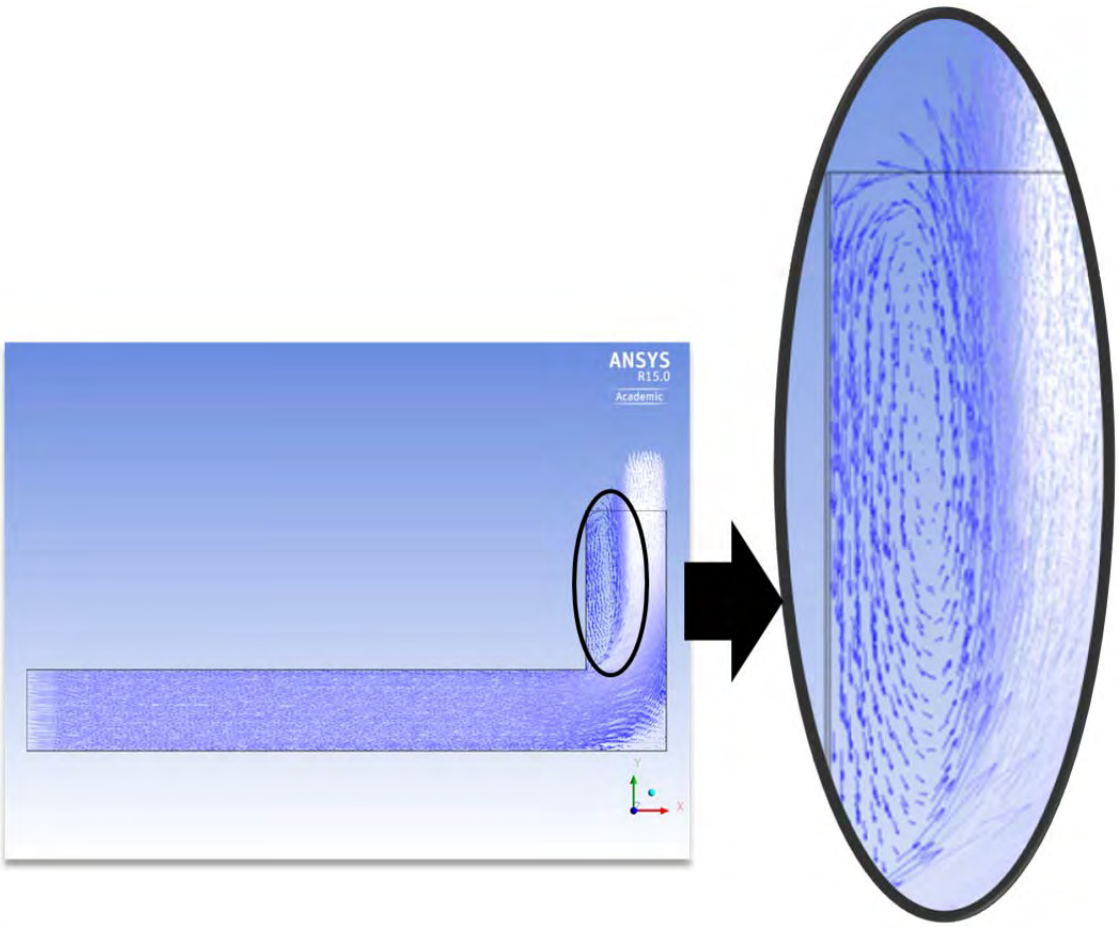


Figure 17 Secondary recirculation zone on wall $Q_3$; $h_{ext}$=5 W/m$^2$K ($h_{ext}$*=4.27 x 10–$^2$), L*=4, H*=1.5, l*=0.25, Re=20,000 (MEP-803A)

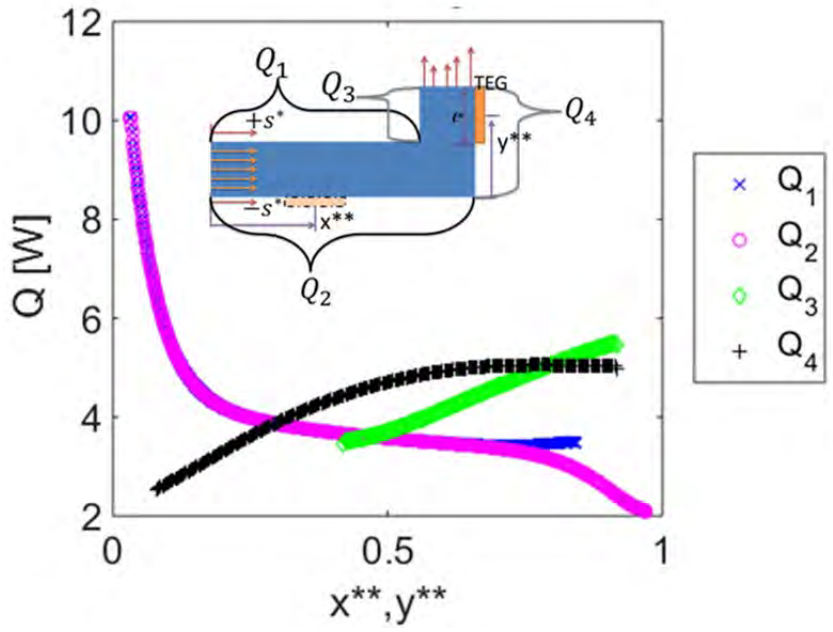


Figure 18 Effect of WHR device placement (x**, y**) on Q [W] for $h_{ext}$=5 W/m$^2$K ($h_{ext}$*=4.27 x 10$^{-2}$), L*=4, H*=1.5, l=25 cm (l*=0.25), Re=20,000 (MEP-803A—dimensional heat transfer values)

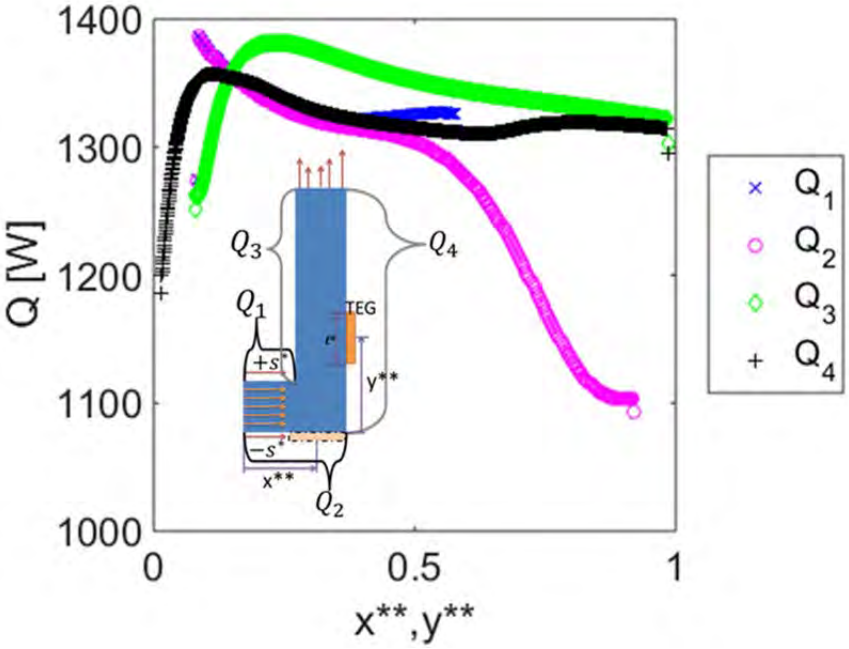


Figure 19 Effect of WHR device placement (x**, y**) on Q [W] for $h_{ext}$=5 W/m$^2$K ($h_{ext}$*=8.54 x 10$^{-4}$), L*=1.5, H*=8, l=25 cm (l*=0.25), Re=1,000,000 (LM2500—dimensional heat transfer values)

## 2. Inlet Reynolds Number and Local Reynolds Number Depression Mixing

In order to understand the importance of the inlet Reynolds number and local Reynolds number depression effect, one model was run at both low (20,000) and high (1,000,000) Reynolds numbers. L*=1.5 and H*=8 for this model. Figure 20 shows the non-dimensional wall heat flux for both cases. The non-dimensional heat flux as represented by $\Theta$ is the fraction of maximum heat flux. The maximum heat flux is for the higher Reynolds number model. Heat flux is considered negative in the direction out of the model, and maximum heat flux is the maximum of the absolute value of heat flux.

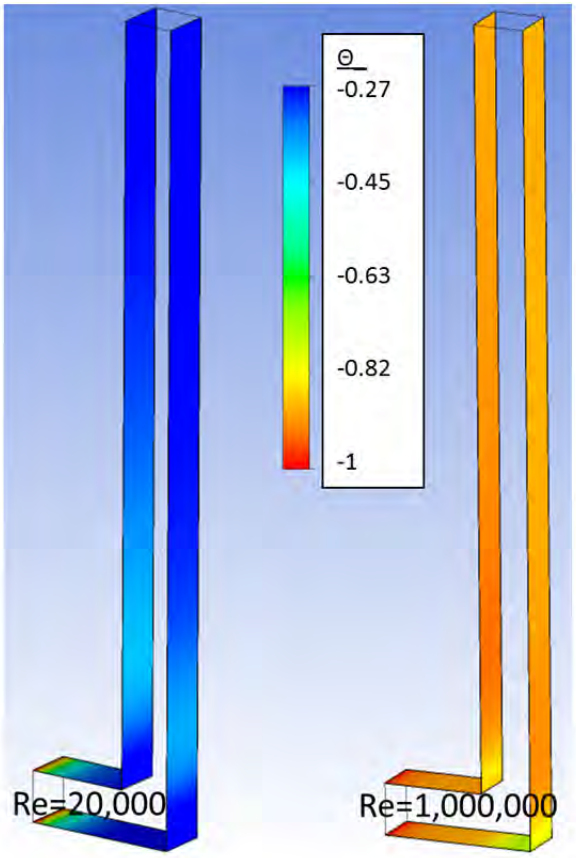


Figure 20 Non-dimensional heat flux ($\Theta = \frac{q"}{q"_{max}}$) comparison: Re=20,000 ($h_{ext}$*=4.27 x 10$^{-2}$) vs. Re=1,000,000 ($h_{ext}$*=8.54 x 10$^{-4}$); $h_{ext}$=5 W/m$^2$K, L*=1.5, H*=8 (Note: $q"_{max}$ is the maximum value of both configurations)

Figure 21 and Figure 22 show the secondary recirculation zone and wall heat flux for Reynolds numbers of 1,000,000 and 20,000, respectively. The areas of maximum heat flux local to the secondary recirculation zone occur where the flow turns toward wall $Q_3$ for both high and low Reynolds number cases. Note that the non-dimensional velocity u* is nearly the same in both cases, but the heat flux profile is different for each case. The heat fluxes in each of these figures are normalized by the local maximum heat flux in each model in order to show the maximum value in each. The heat fluxes for the majority of the low Reynolds number case are much smaller than the peak heat flux, and the average heat flux in the region of the secondary recirculation zone for the high Reynolds number case is closer to its peak heat flux. The heat flux in the high Reynolds number model is more uniform ($\Theta = -0.74$ to $-1$) throughout with most values falling within 10% of the maximum value. While the heat flux profile is different for each case, the geometry imposes similar areas of peak and minimum heat fluxes.

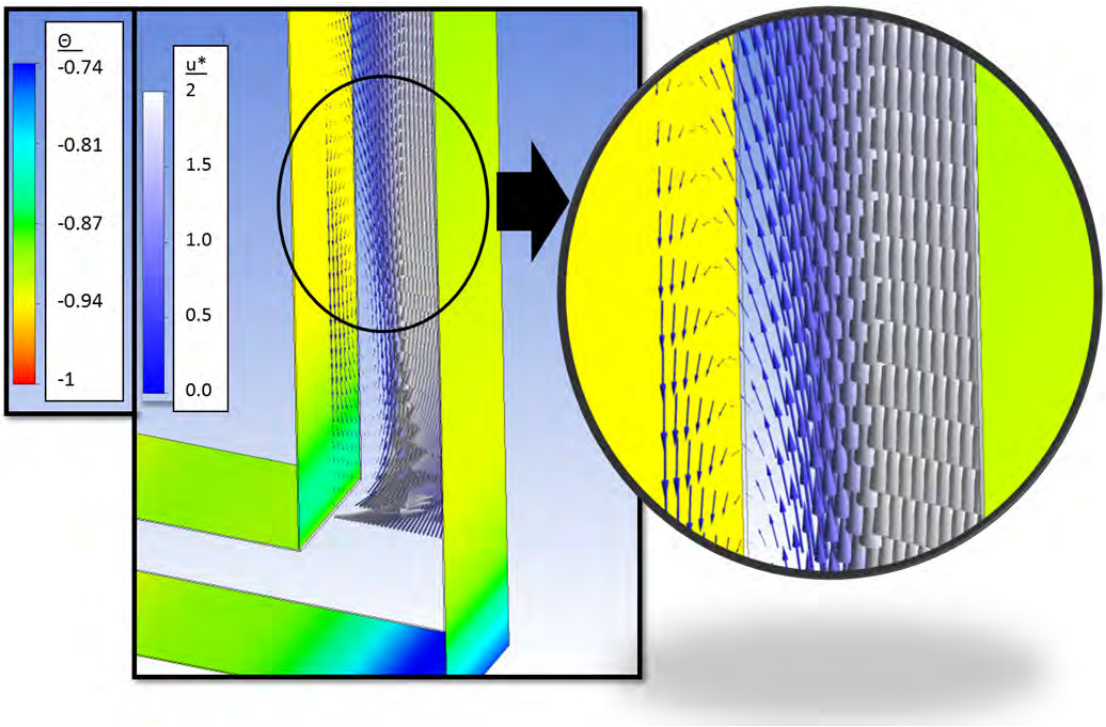


Figure 21 Velocity vectors in vicinity of secondary recirculation zone, heat flux relative to this diagram; $h_{ext}$=5 W/m$^2$K ($h_{ext}$*=8.54 x 10–$^4$), L*=1.5, H*=8, Re=1,000,000

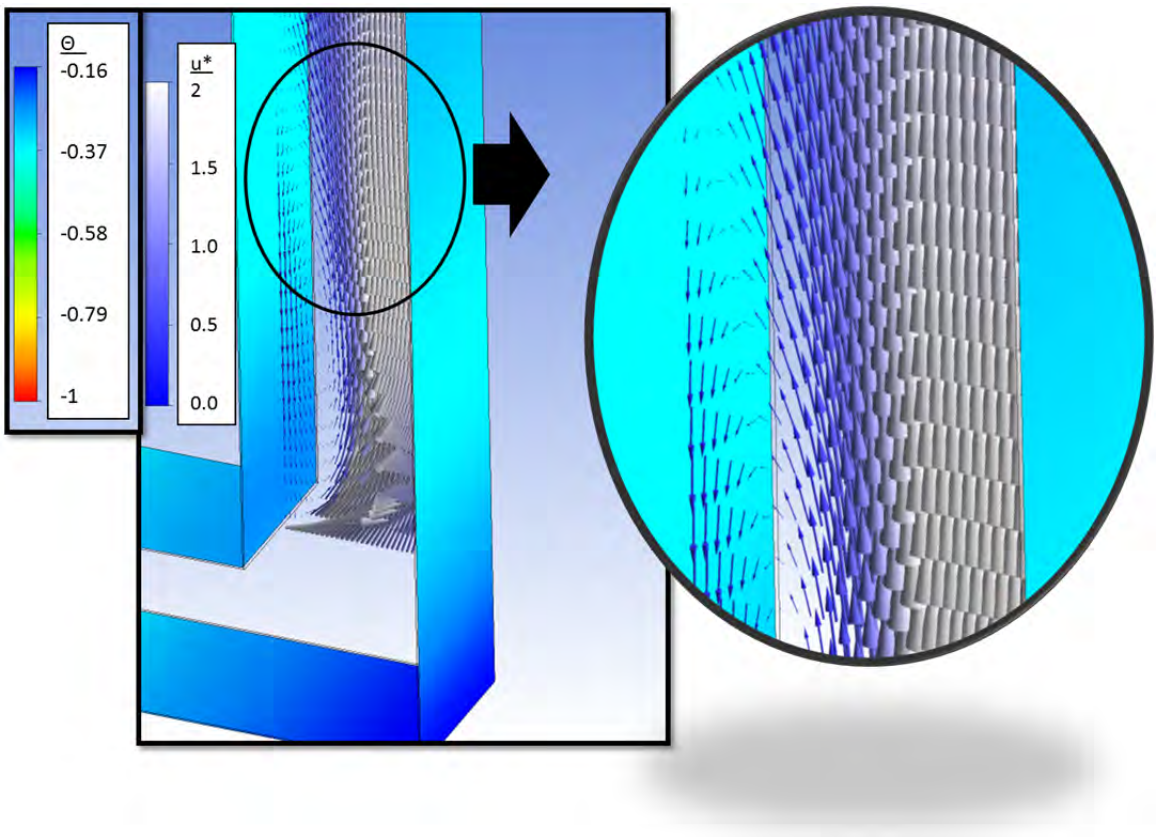


Figure 22 Velocity vectors in vicinity of secondary recirculation zone, heat flux relative to this diagram; $h_{ext}$=5 W/m$^2$K ($h_{ext}$*=4.27 x 10–$^2$), L*=1.5, H*=8, Re=20,000

When the fluid temperature fields are compared side by side (see Figure 23) it becomes apparent why the average heat flux is greater for the high Reynolds number case. The temperature field for the high Reynolds number case is much more uniform due to higher levels of turbulence and mixing. The absolute speed of rotation of the secondary recirculation zone is higher and allows for the hot centerline gas to quickly replenish gas that experiences a drop in temperature near the wall ($\theta \approx 1$ indicating almost no temperature drop) . In contrast, the recirculation zone rotation is much slower for the low Reynolds number case, and hot exhaust gases spend more time next to wall $Q_3$. This explains the much larger heat flux gradient in the low Reynolds number case near the secondary recirculation zone. This finding indicates that the consideration of WHR device placement for maximum heat recovery near this region is extremely important for low Reynolds number applications. The heat transfer is only meaningfully enhanced near

the top of the recirculation zone. A WHR device placed near this region would also experience larger temperature gradients which could lead to early failure from thermal stress.

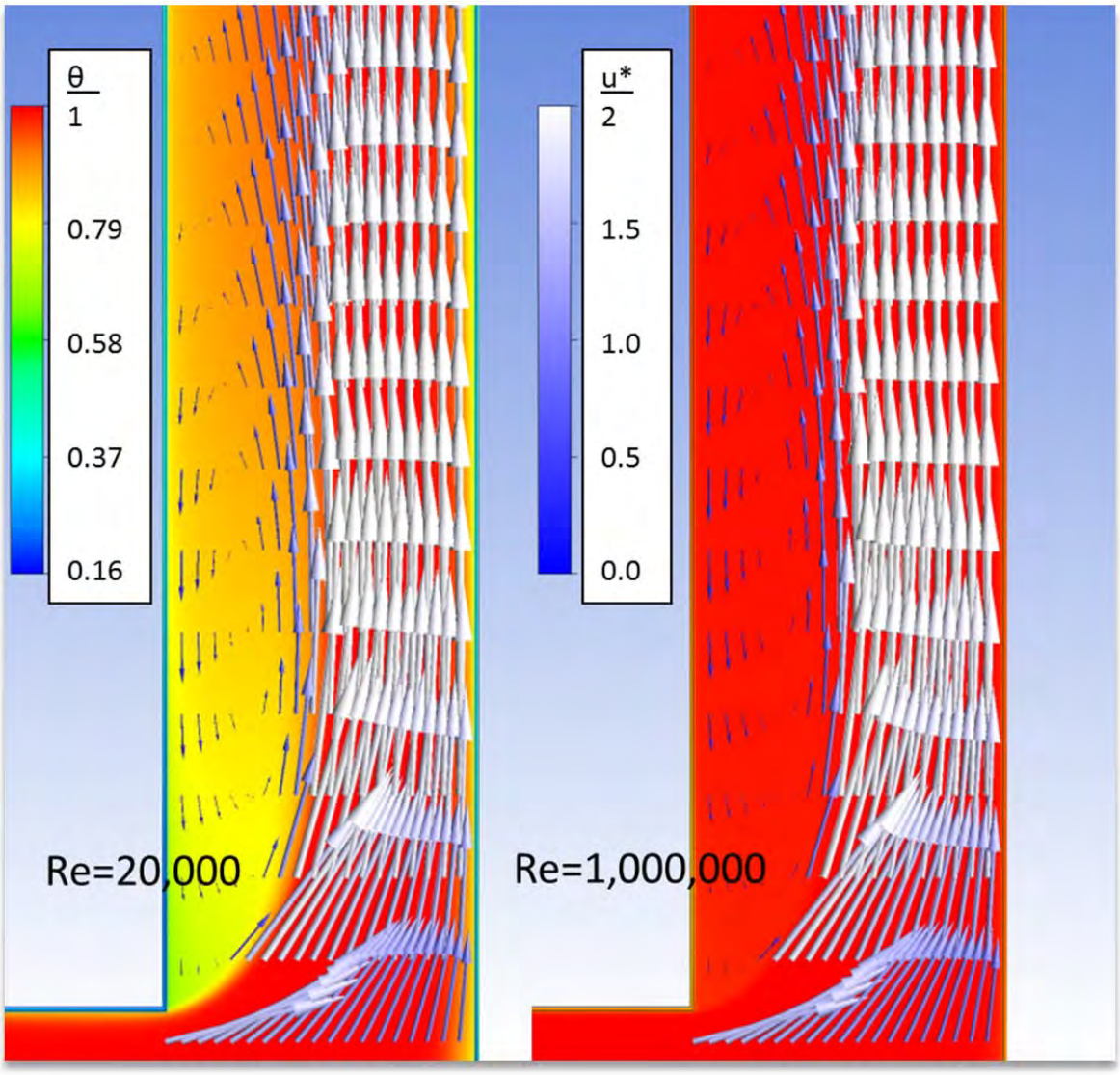


Figure 23 Temperature field comparison: Re=20,000 ($h_{ext}$*=4.27 x 10–$^{2}$) vs. Re=1,000,000 ($h_{ext}$*=8.54 x 10–$^{4}$); $h_{ext}$=5 W/m$^{2}$K, L*=1.5, H*=8

For high Reynolds number applications, the wall heat flux is more uniform. WHR device placement within the secondary recirculation zone actually enhances overall external heat transfer.

### 3. Device Size

For device size, both types of models show some sensitivity, but the low Reynolds number model shows that changes in device size in certain areas do not produce substantial gains in heat recovery. Figure 24 illustrates this nicely. Take, for example, a point along wall $Q_4$ near s*=-1 and l*=0.50. Say after installation it was found that the heat recovery from the device at this location was not satisfactory and needed to be increased. One option would be to increase the device size. Note that increasing the device size from an l* value of 0.50 to 0.75 (50% increase) at this location results in approximately a two-thirds increase in heat recovery; however, notice that a minor shift in position (more negative s*) produces nearly the same result! System designers should use this type of analysis to help determine whether an increase in WHR device size (and cost) is truly necessary and beneficial. Note that geometry is that of the LM2500 model but Reynolds number is set to 20,000 for comparison with Reynolds number of 1,000,000 in Figure 25.

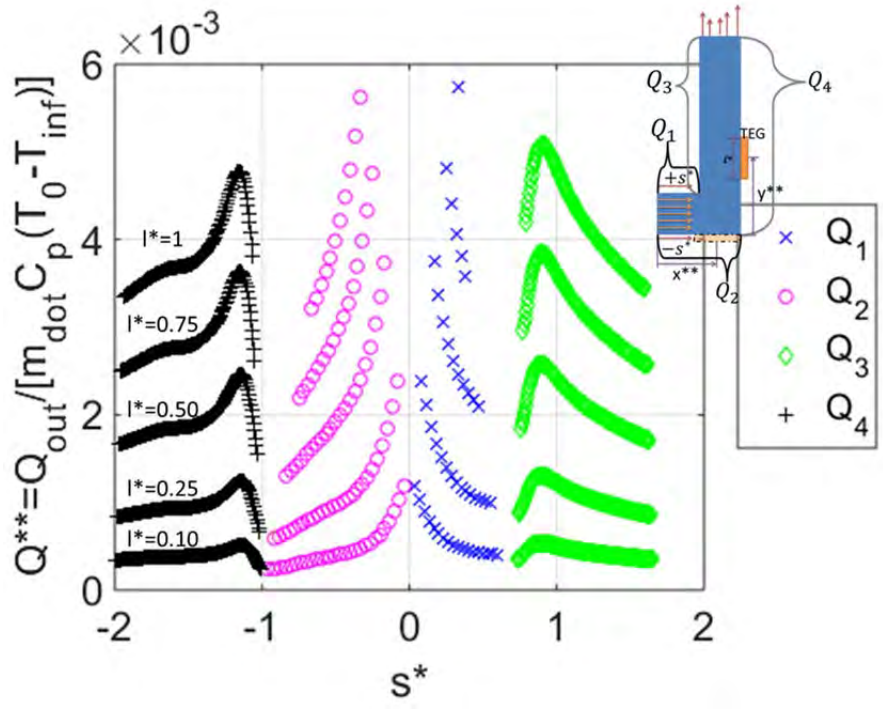


Figure 24 Effect of WHR device size (l*=0.1 to 1) and placement (s*) on Q** for $h_{ext}$=5 W/m$^2$K ($h_{ext}$*=4.27 x 10–$^2$), L*=1.5, H*=8, Re=20,000 **(Variable l*)**

In the high Reynolds number case shown in Figure 25, the change in heat transfer rate from increases in WHR device size do not overlap with changes in WHR device position. As mentioned previously, this is due to the more uniform heat flux due to better fluid mixing associated with higher Reynolds number flows. The dimensions of the model in Figure 25 are indicative of those in a shipboard LM2500 exhaust duct.

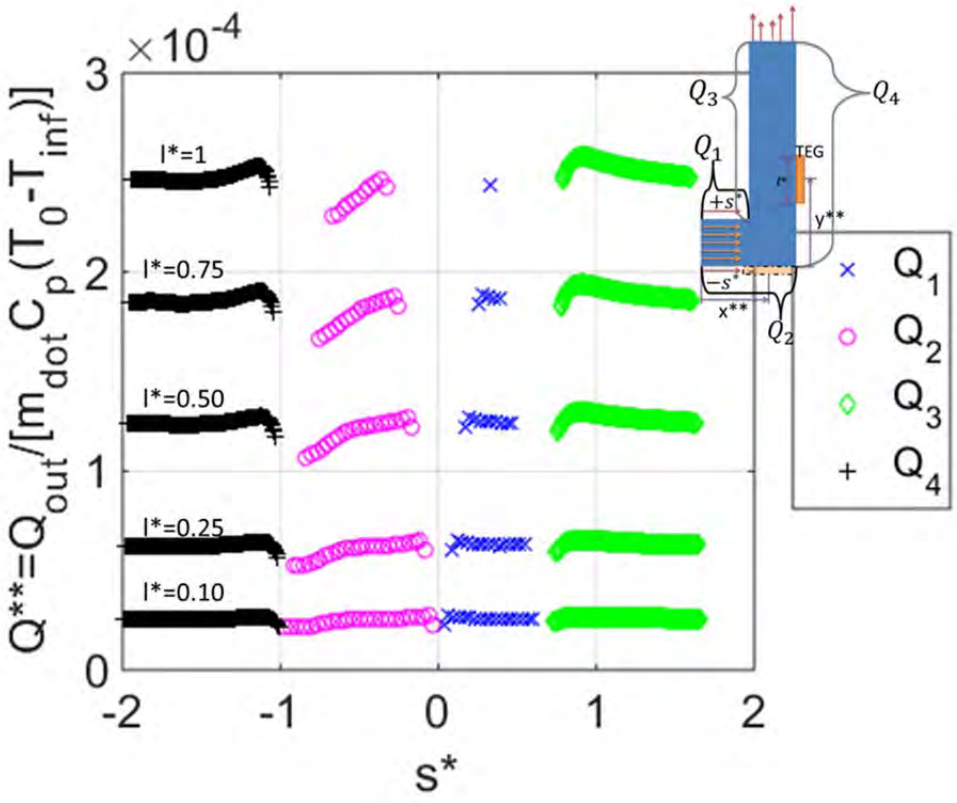


Figure 25 Effect of WHR device size (l*=0.1 to 1) and placement (s*) on Q** for $h_{ext}$=5 W/m$^2$K ($h_{ext}$*=4.27 x 10–$^2$), L*=1.5, H*=8, Re=1,000,000 **(Variable l*)**

Figure 26 is representative of the MEP-803A exhaust duct configuration. It draws similarities to Figure 24 in that increased WHR device size is not the only option for increasing the heat transfer rate along the walls, particularly on walls $Q_1$, $Q_2$, and $Q_4$.

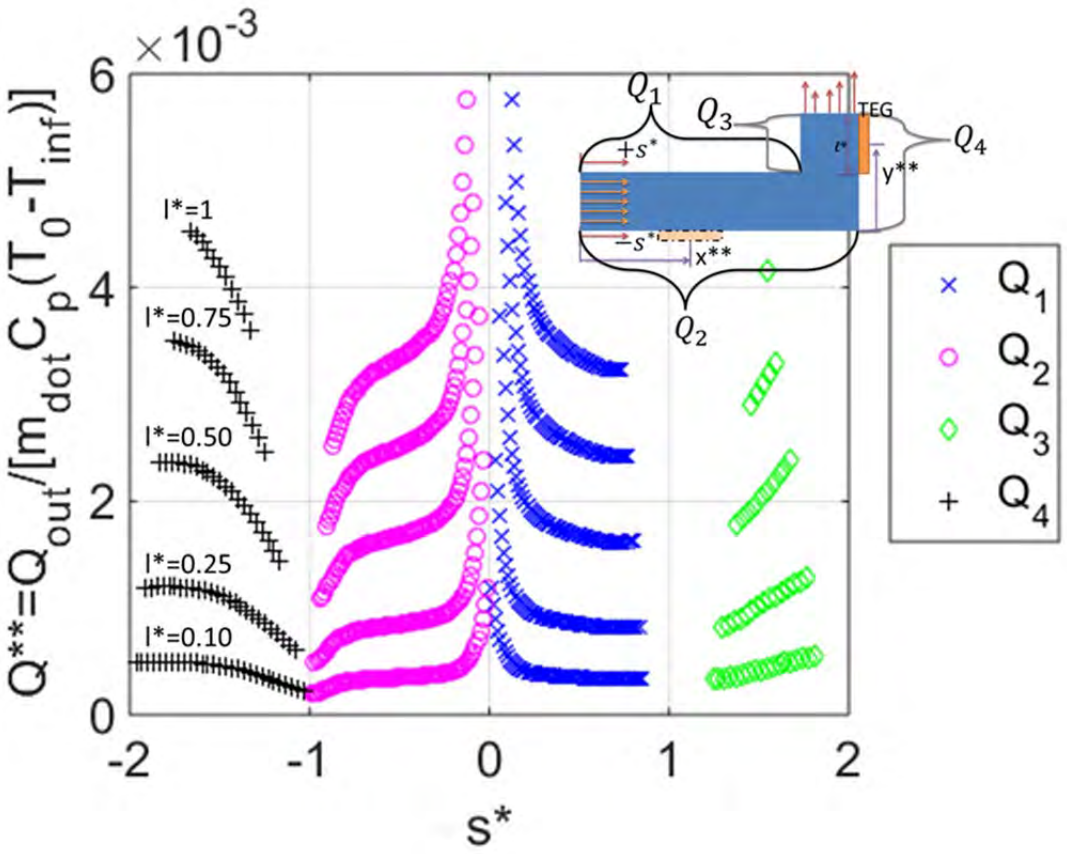


Figure 26 Effect of WHR device size: Q** vs. s*; $h_{ext}$=5 W/$m^2$K ($h_{ext}$*=4.27 x 10–$^2$) , L*=4, H*=1.5, l*=0.1→1, Re=20,000 **(Variable l*)**(MEP-803A)

## C. EFFECT OF GEOMETRY ON HEAT TRANSFER RATE

Because exhaust duct geometries widely vary, it is essential to understand what the effect is of changing duct dimensions. For this thesis, only the inlet and outlet lengths L* and H* were varied. Koh [3] analyzed the effect of changing diameter ratios between a water jacket heat exchanger and an exhaust duct. He found that small diameter ratios optimized heat recovery. Koh also found that larger length to diameter ratios improved heat recovery, so it is no surprise to see increased Q** with increasing L* and H* in Figure 27. What is interesting to note is that as Reynolds number is increased for both the MEP-803A and LM2500 turbulence models, there exists a points where the Q** values at different values of H* and L* begin to overlap. It should be noted here that for turbulent models the top of the secondary recirculation zone is approximately at 4d or 2$D_h$ above the bend outer wall, which is longer than the exit portion of the MEP-803A model. As the

Reynolds number and turbulent kinetic energy increase, more energy that could have been captured through the wall escapes through the outlet. This is more pronounced when the secondary recirculation zone height is taller than H*. As both the Reynolds number and H* grow larger, the incremental change in H* becomes less and less important and the results begin to merge at very high Reynolds number. This is due to the well mixed flow and long H* lengths which allows more time for heat transfer to occur.

Small values of L* are representative of gas turbine prime movers for naval applications such as the LM2500 or MT-30. Larger L* values may be more representative of applications for naval base power plants utilizing LM2500 or LM100 series gas turbines.

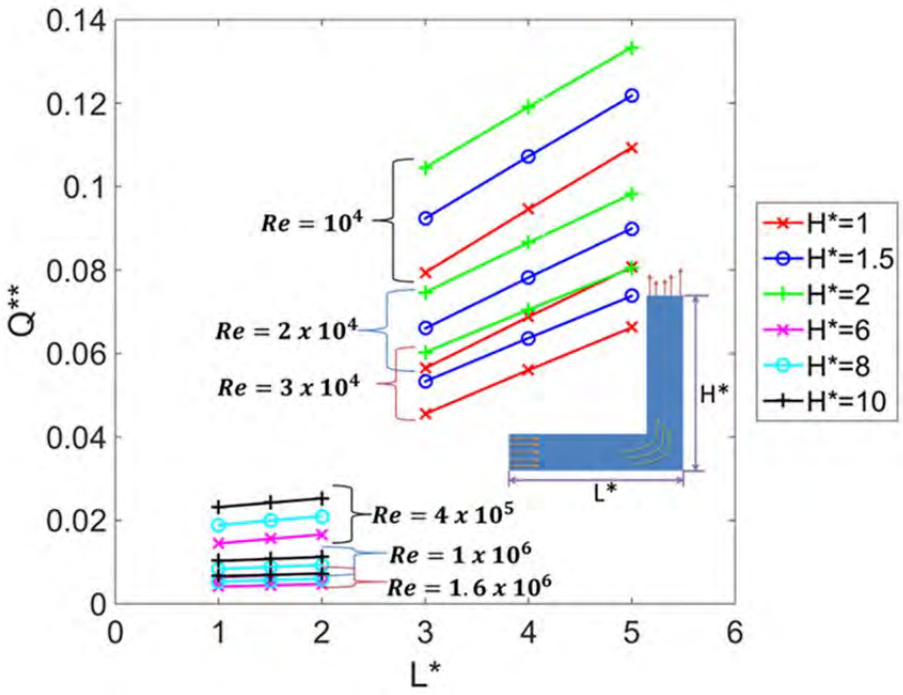


Figure 27 Effect of changes in L*, H*, and Re on heat recovery rate; $h_{ext}$=5 W/m$^2$K ($h_{ext}$*=8.54 x 10$^{-2}$ to $h_{ext}$*=5 x 10$^{-4}$)

## D. EFFECT OF REYNOLDS NUMBER ON HEAT TRANSFER RATE

Reynolds number was varied from 10,000 to 30,000 for the MEP-803A models and 400,000 to 1,600,000 for the LM2500 models. As indicated by Figure 28, the non-

dimensional heat transfer rate, Q**, is less sensitive to changes in Reynolds number for the LM2500 than for the MEP-803A. Notice that even though the range of Reynolds numbers is larger for the LM2500, the absolute change in Q** is smaller. It was found that as Reynolds number increased, Q** decreased (see Figure 28). The exhaust inlet length L is longer than the exhaust length exit H for the MEP-803A, and L is shorter than H for the LM2500, so it is no surprise that the values of Q** are higher for the LM2500 on walls Q3 and Q4. This suggests that Q**(Re) is a decaying function that resembles a power law and that changes to Q** are much more sensitive to Reynolds number at lower values of Reynolds number. All numerical curves in Figure 28 follow the form:

$$Q^{**} = \mathrm{CRe}^{-1/2} \tag{33}$$

The constant C varies depending from which wall Q** is being measured and the external heat transfer coefficient. Based on the definition of Q** (Equation (17)):

$$q'' \propto Q^{**}\dot{m} \tag{34}$$

$$q'' \propto Q^{**}Re \tag{35}$$

Based on the numerical results and Equation (33) it can be shown that:

$$q'' \propto CRe^{1/2} \tag{36}$$

It is known from literature [6] that heat flux is proportional to Nusselt number, so it can be concluded in this case that:

$$Nu \propto Re^{1/2} \tag{37}$$

This is the right form for Reynolds number dependence in classical heat transfer work where $Nu \propto Re^{n}$ and n varies from $\frac{1}{5}$ to $\frac{4}{5}$ for similar internal flows [6].

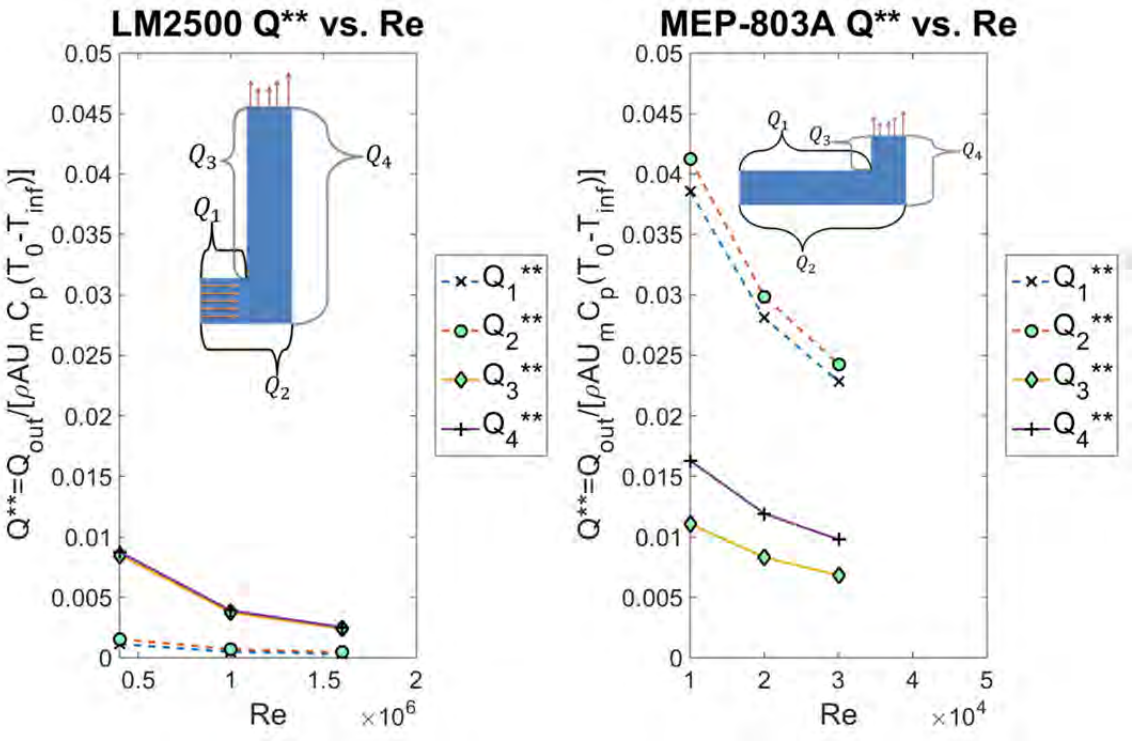


Figure 28 Effect of Reynolds number on Q** for $h_{ext}$=5 W/m$^2$K ($h_{ext}$*=8.54 x 10–$^4$), L*=1.5,H*=8 (LM2500) and $h_{ext}$=5 W/m$^2$K ($h_{ext}$*=4.27 x 10–$^2$), L*=4,H*=1.5 (MEP-803A)

## E. COMBINED EFFECT OF REYNOLDS NUMBER AND EXTERNAL HEAT TRANSFER COEFFICIENT ON HEAT TRANSFER RATE

As already noted, the heat transfer rate becomes less sensitive at very high Reynolds numbers, but there is another parameter that becomes more sensitive. As the Reynolds number becomes large there is more sensitivity to changes in external heat transfer coefficient. Figure 29 covers all the Reynolds number ranges encountered in prime movers, at-sea generators, and mobile generator sets (MEP-803A, Allison 501K, LM2500, MT-30) as well as shore-based power stations (LM2500, LM100). Reynolds number flows on the order of $10^4$ such as the MEP-803A, improve their heat recovery rate by 25% by doubling the external heat transfer coefficient. On the other hand for large Reynolds number flows such as the LM2500 or LM100, doubling the external heat transfer coefficient results in a 91% improvement to heat recovery! Table 3 provides a tabular view of this trend which is also shown in Figure 30. The green box outlines the area where the change in external heat transfer coefficient sensitivity is most rapid.

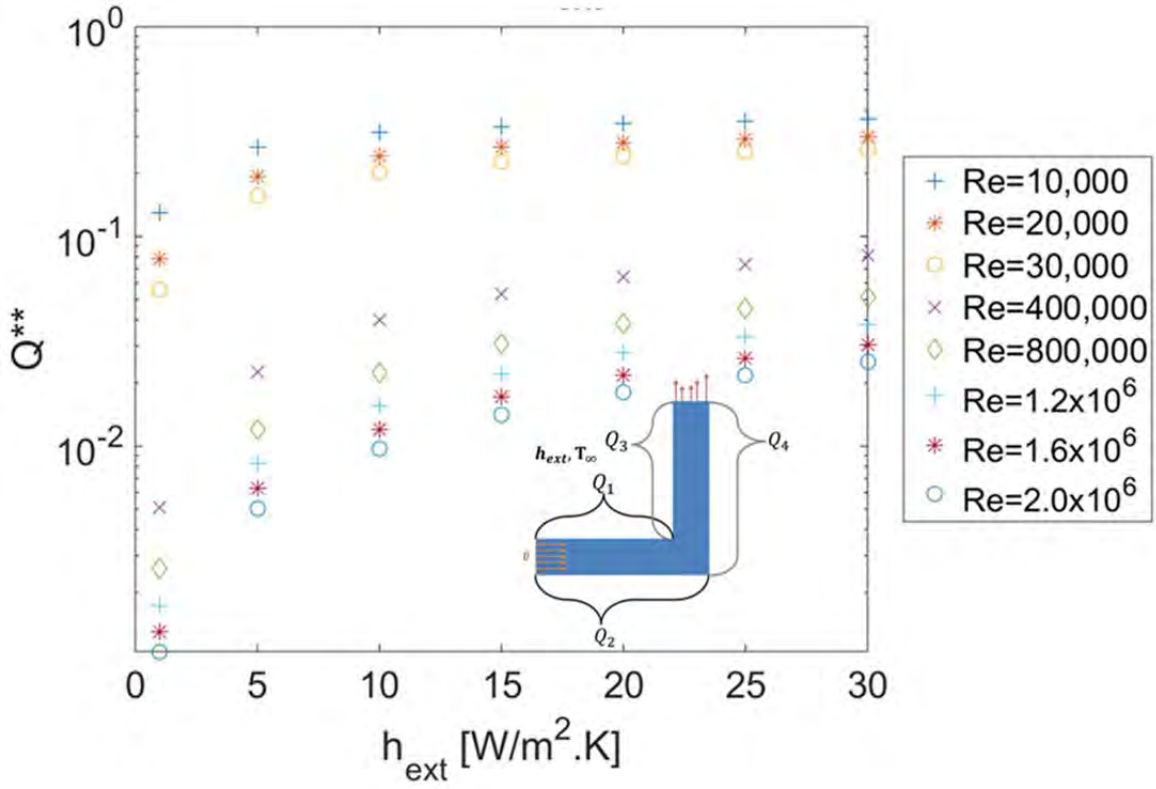


Figure 29 Combined effect of Reynolds number and external heat transfer coefficient on Q** for L*=10, H*=6.5

The takeaway here is that WHR devices that employ expensive, high heat transfer coefficient heat exchangers, such as the S-$CO_2$ system designed by Concepts NREC [11], are most effective in high Reynolds number flows on the order of $10^5$ and above such as the LM2500. Placing an expensive heat exchanger on an engine such as the MEP-803A would not yield the same improvement in heat recovery. For engine exhaust ducts that operate in the Reynolds number range from $10^4$ to $10^5$, important design decisions must be made regarding the tradeoffs between performance and cost when picking a proper heat exchanger. An engine that operates near the higher end of the spectrum would certainly benefit from an improved heat exchanger while one operating at the lower end would clearly not benefit near as much. An effective increase in external heat transfer coefficient can be brought about by using something as simple as finned extensions.

Table 3 Ratio of percent change in heat recovery rate to percent change in external heat transfer coefficient from 5 to 10 W/m$^2$K for various Reynolds numbers; L*=10, H*=6.5

| Re | Q** at hext=5 W/m$^2$K | Q** at hext=10 W/m$^2$K | $\%\Delta Q^{**} / \%\Delta h_{ext}$ |
|---|---|---|---|
| $10^4$ | 0.2676 | 0.3131 | 0.17 |
| 2.0 x $10^4$ | 0.1943 | 0.2424 | 0.25 |
| 3.0 x $10^4$ | 0.156 | 0.2039 | 0.31 |
| 4.0 x $10^5$ | 0.02263 | 0.03976 | 0.76 |
| 8.0 x $10^5$ | 0.01206 | 0.02224 | 0.84 |
| 1.2 x $10^6$ | 0.008246 | 0.01553 | 0.88 |
| 1.6 x $10^6$ | 0.00627 | 0.01195 | 0.91 |
| 2.0 x $10^6$ | 0.005061 | 0.009721 | 0.92 |

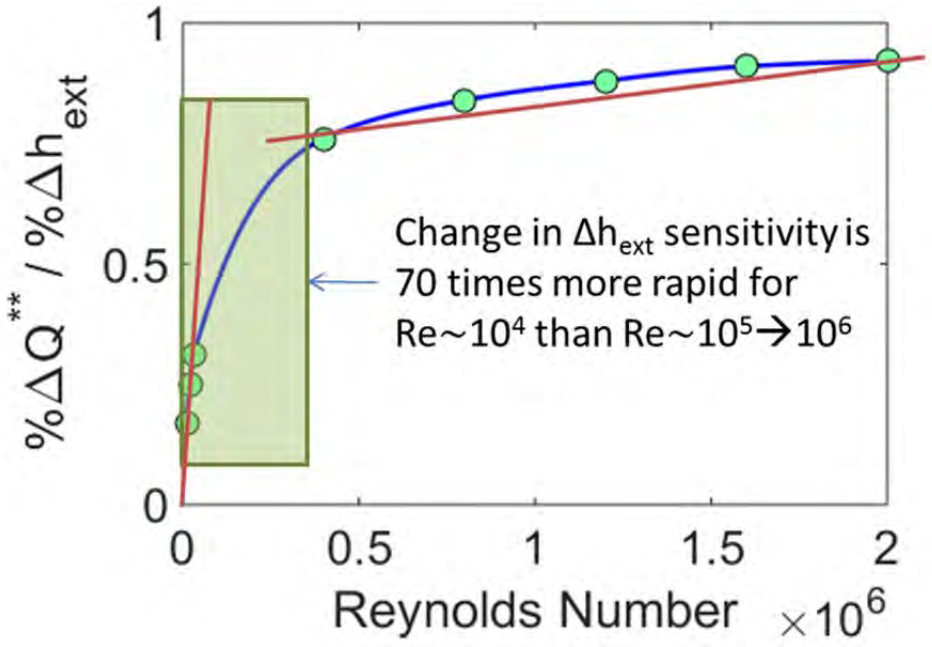


Figure 30 Ratio of percent change in heat recovery rate to change in external heat transfer coefficient from 5 to 10 W/m$^2$K for various Reynolds numbers; L*=10, H*=6.5

## F. PARAMETERS AFFECTING EXHAUST BULK EXIT TEMPERATURE AND IR SIGNATURE

It is desirable to use a WHR device to not only recover heat but to also lower the mixing cup temperature of the gas exiting the exhaust. Lowering the mixing cup temperature will decrease the amount of heat given off as radiation and thereby decrease the intensity of the IR signature in the bandwidths of interest to enemy weapons. In order to study the drop in mixing cup temperature, the size of the WHR device was parameterized. Using the results from Section III.B.1, a WHR device of l*=0.25 was placed at the point of maximum heat recovery on each wall, and its size was expanded in both directions parallel to the wall until its length was equal to or nearly equal to the total length of the wall. This process was carried out for all four walls at overall external heat transfer coefficients, U, of 10 W/m$^2$K, 100 W/m$^2$K, and 1000 W/m$^2$K totaling 193 unique design points. Overall external heat transfer coefficients were specified to show applicability to any materials with variable thermal conductivity and variable convection conditions. The overall external heat transfer coefficient includes the thermal conductivity of the exhaust duct wall and the external heat transfer coefficient.

$$U = \frac{1}{\frac{t}{k_{wall}} + \frac{1}{h_{ext}}} \tag{38}$$

### 1. Reynolds Number, Heat Transfer Coefficient, and Device Size

Figure 31 shows both the LM2500 model and MEP-803A model depicting the effect of device size to wall length ratio on non-dimensional temperature drop. Device size to wall length ratio is the ratio of l* to L* or l* to H* depending on which wall the device is located. Non-dimensional temperature drop is defined by Equation (28).

Although the two models have quite different configurations it is easily noticed that both Reynolds number and device size affect the mixing cup temperature. This is expected since it is known that a larger device will increase heat recovery and decrease the mixing cup temperature, and as mentioned previously, high Reynolds number flows exhibit more sensitivity to changes in external heat transfer coefficient. It can be seen from Figure 31 that lower Reynolds number flows such as the MEP-803A (Re~$10^4$) do

not experience a significant drop in mixing cup temperature for increased WHR device sizes. Although temperature drop is larger across the board for the MEP-803A model, the LM2500 model temperature drop is much more sensitive to changes in device size and external heat transfer coefficient. This makes sense based on the results from Section III.E and because the heat flux in higher Reynolds number flows (Re~$10^6$) is more uniform. Neither case provides substantial reduction in mixing cup temperature, so additional ideas must continue to be explored to reduce IR signatures.

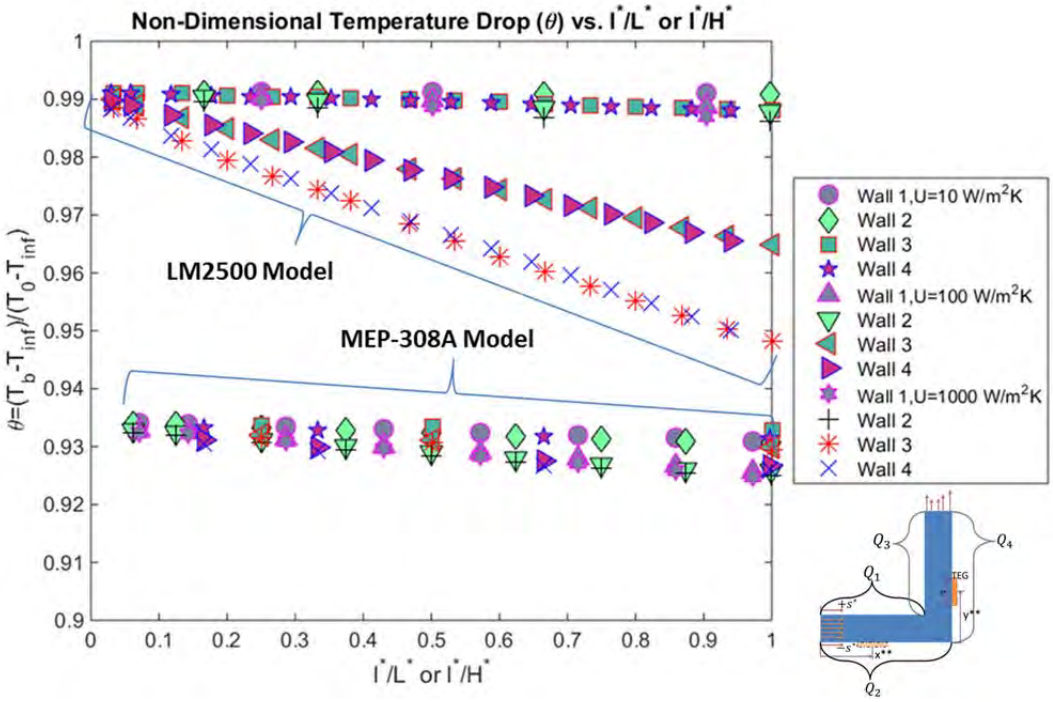


Figure 31 LM2500 (L*=1.5, H*=8) and MEP-803A (L*=4, H*=1.5) models: Effect of device size to wall length ratio and overall external heat transfer coefficient on non-dimensional temperature. $\theta = 1$ means that the temperature of the exhaust gas is equal to the exhaust inlet. The overall external heat transfer coefficient, U, includes the thermal conductivity of the exhaust duct wall and the external heat transfer coefficient

### 2. Device Placement: Wall Selection for IR Reduction

Device placement and wall selection are closely related to all of the parameters that have been discussed, especially external heat transfer coefficient, geometry

definition, and device size, but it is worth mentioning it separately here again to highlight how important wall selection is to the mixing cup temperature drop. Notice immediately in Figure 31 that placement and size of the WHR device at any wall and position has almost no practical effect on lowering the mixing cup temperature for either case, but the physics involved are still worthy of discussion for scientific interest.

Recall the secondary recirculation zone for MEP-803A model and how its flow exits the exhaust duct so only a small portion of flow has the chance to impinge on the inner wall and increase the heat transfer rate (see Sections III.B.1 and III.B.2). Even when a WHR device covers 100% of the wall length, it does little to reduce the IR signature intensity. Conversely, note for the LM2500 model a device placed on either wall $Q_3$ or $Q_4$ has a much more sizeable contribution to IR signature intensity reduction. In fact, a device on wall $Q_4$ outperforms placement on walls $Q_1$ and $Q_2$.

Recalling that the high Reynolds number models such as the LM2500 are very sensitive to changes in external heat transfer coefficient (Section III.E), notice how there is little appreciable change in the outlet mixing cup temperature when the overall external heat transfer coefficient is high and even when the WHR device covers the entire length of any of the walls; but increasing the overall external heat transfer coefficient from 10 $W/m^2K$ to 100 $W/m^2K$ has a much larger effect on lowering the mixing cup temperature for the LM2500 model. Also notice that in this case where the geometry of the outlet region is much longer than the MEP-803A model, walls $Q_3$ and $Q_4$ are good places for placing the WHR device in order to reduce IR signature intensity. Walls $Q_1$ and $Q_2$, because of their relatively short length and rapidly developing thermal boundary layers provide little temperature reduction with increased overall external heat transfer coefficient.

To illustrate the impact of a WHR device placed in an optimal location, consider an example. Place a WHR device on wall $Q_4$ with a heat exchanger with an overall external heat transfer coefficient of 1000 $W/m^2K$. Assume that the rest of the exhaust duct is well insulated to protect surrounding equipment (i.e., aboard a ship). Say the heat

exchanger covers roughly 12% of wall $Q_4$, which on a 15 m (50 ft) stack would be about 1.8 m (6 ft), and the inlet exhaust temperature is approximately 600 K.

This configuration would reduce the exhaust exit mixing cup temperature to approximately 595 K. Solving Equation (1) shows that the average spectral emissive power is reduced by 4.06%. If the gas was considered to radiate as a blackbody (which is not the case), integration of Equation (1) at the mixing cup temperature over the thermal spectrum shows a decrease in the total emissive power from thermal radiation by 4.15%.

Table 4 shows that even under ideal conditions with the WHR device covering 100% of wall $Q_3$ with an overall external heat transfer coefficient of $1000 W/m^2K$, the reduction in total emissive power from thermal radiation in only 14.08%. For shipboard applications, this would require placing a WHR device along the entire length of the exhaust duct from the engine room to the highest level of the ship. Anyone familiar with surface ships will realize this would not be practical or even possible without a major overhaul, high costs, and added weight high above the center of gravity which is bad for ship stability.

It is also important to note that these temperature drops are stated for the mixing cup temperature, which only gives a feel for the enthalpy average temperature change of the flow. The maximum intensity of emissive power will be determined by the maximum temperature in the flow, which is relatively unchanged for each case, meaning that the IR signature of peak intensity is unchanged.

Table 4 $\Delta E_b$ at selected walls and overall external heat transfer coefficients

| $T_0$ (K) | $\theta$ | U ($W/m^2K$) | Wall | l*/L* | l*/H* | $T_b$ (K) | $\Delta E_b$ |
|---|---|---|---|---|---|---|---|
| 600 | 0.9483 | 1000 | $Q_3$ | - | 1.0 | 584 | -14.08% |
| 600 | 0.9763 | 100 | $Q_4$ | - | 0.5291 | 593 | -5.87% |
| 600 | 0.9837 | 1000 | $Q_4$ | | 0.1176 | 595 | -4.15% |
| 600 | 0.9886 | 1000 | $Q_2$ | 0.3322 | - | 597 | -2.47% |

The takeaway from these findings is that while a WHR device of the type studied in this thesis can aid in reducing the IR signature intensity of an engine exhaust, the effect is very small. It is small even when device size to wall length ratio and overall external heat transfer coefficients are very high. It would behoove a USN acquisition program manager to be weary of claims that a commercial WHR device can significantly reduce IR signature without taking up significant real estate or inducing large pressure drops in the flow.

# IV. CONCLUSIONS

## A. OBSERVATIONS AND RECOMMENDATIONS

Engine exhausts contain extremely complex flow patterns. The flow patterns studied in this thesis are more basic representations of these complex flows yet they reveal features that would prove to be useful while making design decisions. The analysis of heat transfer and fluid flow in a 2-D 90-degree miter bend highlights the major parameters affecting WHR by removing some of the complexity without losing the essence of the problem. The turbulent models validated in the thesis directly support NPS WHRS Roadmap objectives and will serve as the baseline for further research in WHRS by NPS students. Specifically this research meets the Roadmap (2014–2020) objectives aligned with building, running, and understanding thermal and turbulence models and their capabilities. This study provides first-of-its-kind insight into how to optimally place a WHR device, it adds to the body of knowledge used for studying thermal stresses in WHR devices, and it contributes in a meaningful way to NPS's knowledge base for IR signature reduction.

### 1. Counterintuitive Findings Due to Local Reynolds Number Depression

Finding the area of highest heat transfer on the models is not as intuitive as first thought, especially in the higher Reynolds number flows (~$10^6$). It makes sense that the areas closest to the exhaust inlet would have very good heat transfer given the thermally developing boundary layers, and one could probably guess that there would be hot spots on the bend outer wall from the impingement of the main flow. However, the most counterintuitive result was finding a near global-maximum heat transfer rate (in the high Reynolds number case, ~$10^6$) on the bend inner wall after the flow turned the 90-degree bend (on wall $Q_3$). Initially, it was thought that this wall would inhibit heat transfer because of the recirculation zone created from separation of the flow going around the sharp corner. However, this recirculation zone causes a second impingement of the main flow on the inner wall and it slows the flow down causing a local depression in Reynolds number. This allows for enhanced heat transfer because the fluid spends longer traversing

the wall in the thin thermal boundary layer. Though counterintuitive, for the LM2500 model at $1.5D_h$ from the corner of the 90-degree bend inner wall $Q_3$ becomes the most optimal place for maximizing heat recovery due to the effects of the secondary recirculation zone.

### 2. WHR Device Placement and Size

WHR device placement and size are important for several reasons. The placement and size of a WHR device affects not only that amount of heat that can be recovered but also the life of the WHR device. At low Reynolds number (~$10^4$) with small $\zeta^*$ (H/L), heat recovery is maximized by placing a WHR device as close to the exhaust inlet as possible. Near the exhaust inlet a nominally-sized device can recover 75% more energy than the next best option on another wall. Additionally, small changes in position relative to the length of the duct can increase heat transfer to a WHR device significantly (10–70% improvement depending on geometry). Care must be taken when placing a WHR device or any kind of equipment in the areas that show high temperature gradients. These gradients have the potential to induce high thermal stresses in WHR devices and other sensitive equipment installed in or on exhaust ducts. Some of the areas with peak heat transfer exhibit the highest temperature gradients. An attempt to maximize WHR by installing a WHR device in one of these positions could actually prove detrimental to equipment life and be a very costly decision.

### 3. Relationship between Reynolds Number and Duct External Heat Transfer Coefficient

Increased Reynolds numbers improves mixing and overall heat transfer, but the efficiency with which heat from the flow is transferred through the duct walls is reduced. For WHR device designers, it is imperative to understand the relationship between Reynolds number and external heat transfer coefficient to avoid wasting money and resources searching for heat recovery improvements where little is to be gained. This relationship was studied over the entire range of Reynolds numbers encountered in USN and USMC at-sea and shore-based prime movers and generator sets (LM2500, MT-30, MEP-803A, Allison 501K, LM100). Heat recovery improves by more than 90% by

doubling the heat transfer coefficient in high Reynolds number flows (~$10^6$). Low Reynolds number flows (~$10^4$) only improve by 15–25% with the same enhancement. IR signature reduction of 14.08% requires a heat transfer coefficient of 1000 $W / m^2 K$ and an l*/H* value of 1.0. Even with high heat transfer coefficients, non-intrusive WHR devices should not yet be considered as a primary means of IR reduction.

## 4. Importance of Modeling Exact Geometries

In order to maximize heat recovery in any exhaust flow, it is not enough to just improve the heat exchanger properties. In depth full CFD models of engine exhaust flows should be created and analyzed to determine the points of maximum energy recovery, the optimal size (and ultimately cost) of WHR devices, and what places to avoid altogether where flow conditions result in poor heat transfer.

It is clear that areas such as the primary recirculation zone should be avoided along with areas that exhibit extremely high temperature gradients. It is recommended that studies be undertaken to manipulate the flow in order to direct it to more advantageous areas. These flow manipulations could be in the form of baffles or turning vanes as studied by Beale [20] for reducing pressure drop. Besides reducing pressure drop, adding turning vanes could have at least three potentially beneficial effects: (1) direct hot flow toward WHR devices to recapture more thermal energy from the flow, (2) improve thermal gradients in desired areas of exhaust ducts, and (3) WHR devices could be embedded in the turning vanes, taking advantage of developing thermal boundary layers and direct impingement from the main hot flow.

## 5. Implications to Program Managers

DoD researchers and program managers will continue to seek ways to reduce energy usage, but they must be cautious of overstated claims of WHR device capabilities regarding waste heat recovery and/or IR signature reduction. Having a full understanding of what is possible goes beyond just satisfying the second law of thermodynamics. Even when the second law is satisfied, the maximum energy that can be extracted is still only an idealization when the many real-world factors are considered. Exhaust flows require

either very expensive or very intrusive equipment to extract large amounts of waste heat that come with the penalty of either a hefty price tag, reduction in engine performance due to increased pressure drop, or sometimes both.

### 6. Organizational Impact

The USN and DoD must grow and retain organic capabilities to analyze complex engine exhaust flows. This will save the government money and continue to build a pool of experts that can have direct and effective impact on the programs under their charge. The NPS WHRS Team in conjunction with ONR is building and growing this knowledge not only within the talented faculty and DoD contractors at NPS and ONR but among the Naval Officers that are entrusted with the responsibility of overseeing and programming funding for major programs of record within the DoD. The applications extend beyond the WHRS sphere. The USN stands to gain much by growing and retaining corporate technical knowledge in its DoD civilians and Naval Officers that are close to the problems facing the Navy.

## B. IMPACT OF THIS STUDY

The NPS WHRS team is plugged into R&D decisions that are occurring right now in Washington D.C., Naval Surface Warfare Centers, and other facilities that are acquiring technology from commercial sources. This thesis builds on the repository of knowledge for NPS and sets the stage for future studies in WHR. It is another step towards reaching the SECNAV's energy goals for 2020 and beyond. The NPS WHRS team is positioned to be a key player in the future of Navy energy. The impact is this: by laying the groundwork for knowledge buildup in WHRS, the future program managers currently on the NPS WHRS Team and in the NPS Mechanical Engineering Department will be smarter, more capable stewards of American tax dollars when they are in charge of major programs such as WHRS. Ultimately, the Navy benefits.

## C. FUTURE STUDIES

Future studies into WHR, flow manipulation, and thermal stresses in exhaust ducts should be conducted to better understand this critical area. As stated previously,

this thesis only covers some of the most fundamental principles. The following areas are suggested for further research:

### 1. Infrared (Thermal) Radiation and Natural Convection in Exhaust Ducts

This model neglected the effects of radiation and natural convection to simplify the calculations but radiation heat transfer and natural convection can be major players in exhaust flows.

### 2. Effect of Turning Vanes on Heat Transfer

Beale [20] already highlighted the advantages of using turning vanes to reduce pressure drop. Turning vanes could be used to redirect the flow to optimize heat transfer, reduce thermal stresses, or serve as a carrier for WHR devices. This could be especially useful in applications where space to install WHR devices is limited.

### 3. More Complex Geometries and Obstructions, 3-D

Navy platforms have many different exhaust configurations for their prime movers and generators. The DDG-51 class ships employ three 90-degree bends in their exhaust ducting from the LM2500 engines. The current geometry is representative of the first bend immediately after the engine, but there are two more 90-degree bends further up the exhaust stacks that change the flow significantly. The new construction DDG-1000 ships also have a different configuration that should be studied in detail for the future application of WHR devices. Eventually 3-D models should be developed to better understand these complex flows if it is desired to use WHR devices on them.

Exhaust geometries are not always clean like the model in this thesis. There are often obstructions and surface roughness that change flow patterns. For example, the shaft that connects to the MRG runs through the exhaust in some configurations.

### 4. Effect of Turbulence Intensity

In this thesis the turbulence intensity was fixed at 5%. The effect of increasing the turbulence intensity should be studied in more depth to see how it affects parameters such as pressure drop, velocity profiles, exit temperature profiles, and heat transfer.

### 5. WHR Device Development

WHR devices that can be inserted into the flow without causing detrimental pressure drops should be explored in more depth. A WHR device could be embedded in a turning vane, for example. Improving the external heat transfer coefficients at the walls is especially important for high Reynolds number flows. Possibly using an anisotropic material with high thermal conductivities in duct axial directions could help direct more heat toward the WHR device. Graphite may be useful for this application. Cell phone manufacturers use a similar technique with heat spreaders to conduct the thermal energy away from the chips and batteries to the edge of the phone where it can be removed by natural convection.

WHR is an exciting and growing field, and the USN has much to gain from further research in WHRS. It is my hope that this thesis sparks an interest in someone else the same way this topic has for me.

# APPENDIX A. BASIC SETUP AND CAD PARAMETERIZATION

1. Geometry Creation
    a. Define 2D bounds with sketch in Solidworks.
    b. 1st Extrusion: Extrude to width of duct (0.5m)
    c. 2nd Extrusion: Thin feature extrude to create wall (0.005m). Uncheck "merge result."
    d. Save part.
2. CFD Setup
    a. Open ANSYS Workbench from Solidworks menu bar.
    b. In Workbench, drag and drop CFX analysis system onto Solidworks geometry bar.
    c. Create named selections.
    d. Specify meshing parameters.
        i. Sweep method with one sweep division.
        ii. Max size=5mm, Min size=1mm
    e. Enter setup.
    f. Setup BCs.
    g. Select fluid type (Air Ideal Gas)
    h. Solver control
        i. 1000 iterations
        ii. Convergence: RMS 1e-6
        iii. Timescale factor=0.5
3. Solver
    a. Double precision
    b. Platform MPI Local Parallel
    c. Partitions: 8
    d. Current Solution Data (if possible)
4. Parameterize CAD dimensions
    a. Go back to Solidworks
    b. Add "smart dimensions"
    c. Call Primary Dimension "DS_..."
    d. Save
    e. Back to Workbench
    f. Right click geometry and "update from CAD"
    g. Open meshing
    h. Select applicable geometry and "check" the parameter box so "P" is displayed under "CAD Parameters"

There is a nice YouTube video that provides a general outline for the steps above in greater detail. See [31] for details.

## APPENDIX B. ENERGY BALANCE

$$(E_{in} - E_{out}) / E_{in}$$

| Name | L* | H* | $\zeta^*$ | Re | $h_{ext}$ | % Energy Balance |
|---|---|---|---|---|---|---|
| Design Point | | | | | W/(m$^2$K) | |
| DP 0 | 2 | 2 | 1 | 10000 | 5 | -0.0285103 |
| DP 1 | 3 | 1 | 3 | 10000 | 5 | 0.00852975 |
| DP 2 | 3 | 1 | 3 | 20000 | 5 | -0.00266467 |
| DP 3 | 3 | 1 | 3 | 30000 | 5 | -0.00261507 |
| DP 4 | 3 | 1.5 | 2 | 10000 | 5 | -0.0203411 |
| DP 5 | 3 | 1.5 | 2 | 20000 | 5 | -0.00350564 |
| DP 6 | 3 | 1.5 | 2 | 30000 | 5 | -0.00323288 |
| DP 7 | 3 | 2 | 1.5 | 10000 | 5 | -0.0349216 |
| DP 8 | 3 | 2 | 1.5 | 20000 | 5 | -0.0126102 |
| DP 9 | 3 | 2 | 1.5 | 30000 | 5 | -0.00902669 |
| DP 10 | 4 | 1 | 4 | 10000 | 5 | 0.00546189 |
| DP 11 | 4 | 1 | 4 | 20000 | 5 | 0.00391265 |
| DP 12 | 4 | 1 | 4 | 30000 | 5 | -0.00320028 |
| DP 13 | 4 | 1.5 | 2.66667 | 10000 | 5 | -0.0106165 |
| DP 14 | 4 | 1.5 | 2.66667 | 20000 | 5 | -0.00073922 |
| DP 15 | 4 | 1.5 | 2.66667 | 30000 | 5 | 0.0192203 |
| DP 16 | 4 | 2 | 2 | 10000 | 5 | -0.0403423 |
| DP 17 | 4 | 2 | 2 | 20000 | 5 | -0.030061 |
| DP 18 | 4 | 2 | 2 | 30000 | 5 | -0.0114345 |
| DP 19 | 5 | 1 | 5 | 10000 | 5 | 0.00906538 |
| DP 20 | 5 | 1 | 5 | 20000 | 5 | -0.00378829 |
| DP 21 | 5 | 1 | 5 | 30000 | 5 | -0.00364864 |
| DP 22 | 5 | 1.5 | 3.33333 | 10000 | 5 | -0.0218819 |
| DP 23 | 5 | 1.5 | 3.33333 | 20000 | 5 | 0.00478145 |
| DP 24 | 5 | 1.5 | 3.33333 | 30000 | 5 | -0.00476023 |
| DP 25 | 5 | 2 | 2.5 | 10000 | 5 | -0.0444084 |
| DP 26 | 5 | 2 | 2.5 | 20000 | 5 | -0.0199485 |
| DP 27 | 5 | 2 | 2.5 | 30000 | 5 | -0.0145625 |
| DP 28 | 1 | 6 | 0.166667 | 400000 | 5 | -0.00213726 |

| Name | L* | H* | $\zeta^*$ | Re | $h_{ext}$ | % Energy Balance |
|---|---|---|---|---|---|---|
| Design Point | | | | | W/(m$^2$K) | |
| DP 29 | 1 | 6 | 0.166667 | 1000000 | 5 | -0.000972275 |
| DP 30 | 1 | 6 | 0.166667 | 1600000 | 5 | -0.000737296 |
| DP 31 | 1 | 8 | 0.125 | 400000 | 5 | -0.0032131 |
| DP 32 | 1 | 8 | 0.125 | 1000000 | 5 | -0.00136251 |
| DP 33 | 1 | 8 | 0.125 | 1600000 | 5 | -0.000972184 |
| DP 34 | 1 | 10 | 0.1 | 400000 | 5 | -0.00469029 |
| DP 35 | 1 | 10 | 0.1 | 1000000 | 5 | -0.00195623 |
| DP 36 | 1 | 10 | 0.1 | 1600000 | 5 | -0.00107289 |
| DP 37 | 1.5 | 6 | 0.25 | 400000 | 5 | -0.00252384 |
| DP 38 | 1.5 | 6 | 0.25 | 1000000 | 5 | -0.00492238 |
| DP 39 | 1.5 | 6 | 0.25 | 1600000 | 5 | -0.00339891 |
| DP 40 | 1.5 | 8 | 0.1875 | 400000 | 5 | -0.00431409 |
| DP 41 | 1.5 | 8 | 0.1875 | 1000000 | 5 | -0.00165205 |
| DP 42 | 1.5 | 8 | 0.1875 | 1600000 | 5 | -0.00108411 |
| DP 43 | 1.5 | 10 | 0.15 | 400000 | 5 | -0.00535071 |
| DP 44 | 1.5 | 10 | 0.15 | 1000000 | 5 | -0.00258584 |
| DP 45 | 1.5 | 10 | 0.15 | 1600000 | 5 | -0.00700161 |
| DP 46 | 2 | 6 | 0.333333 | 400000 | 5 | -0.00404412 |
| DP 47 | 2 | 6 | 0.333333 | 1000000 | 5 | -0.000644736 |
| DP 48 | 2 | 6 | 0.333333 | 1600000 | 5 | -0.00100108 |
| DP 49 | 2 | 8 | 0.25 | 400000 | 5 | -0.0053289 |
| DP 50 | 2 | 8 | 0.25 | 1000000 | 5 | -0.00210871 |
| DP 51 | 2 | 8 | 0.25 | 1600000 | 5 | -0.000611034 |
| DP 52 | 2 | 10 | 0.2 | 400000 | 5 | -0.00682913 |
| DP 53 | 2 | 10 | 0.2 | 1000000 | 5 | -0.00264959 |
| DP 54 | 2 | 10 | 0.2 | 1600000 | 5 | -0.00636577 |
| DP 55 | 12 | 6 | 2 | 100 | 5 | 0.264536 |
| DP 56 | 12 | 6 | 2 | 10000 | 5 | 0.170262 |

# APPENDIX C. ANSYS REPORTS FOR MEP-803A AND LM2500 MODELS

Note: Cells without a value were variables defined by an expression and specified in ANSYS Workbench parameter sets.

**MEP-308A Model**

Mesh Information for CFX

| Domain | Nodes | Elements | Tetrahedra | Wedges | Pyramids | Hexahedra | Polyhedra |
|---|---|---|---|---|---|---|---|
| Fluid | 202202 | 100000 | 0 | 0 | 0 | 100000 | 0 |
| Solid | 8008 | 2000 | 0 | 0 | 0 | 2000 | 0 |
| All Domains | 210210 | 102000 | 0 | 0 | 0 | 102000 | 0 |

Mesh Statistics for CFX

| Domain | Minimum Face Angle | Maximum Face Angle | Maximum Element Volume Ratio |
|---|---|---|---|
| Fluid | 90 [ degree ] | 90 [ degree ] | 1.00007 |
| Solid | 90 [ degree ] | 90 [ degree ] | 1.00005 |
| All Domains | 90 [ degree ] | 90 [ degree ] | 1.00007 |

Domain Physics for CFX

| Domain - Fluid | |
|---|---|
| Type | Fluid |
| Location | Fluid |
| Materials | |
| Air Ideal Gas | |
| Fluid Definition | Material Library |
| Morphology | Continuous Fluid |
| Settings | |
| Buoyancy Model | Non Buoyant |
| Domain Motion | Stationary |
| Reference Pressure | 1.0000e+00 [atm] |
| Heat Transfer Model | Thermal Energy |
| Include Viscous Dissipation Term | On |
| Turbulence Model | k epsilon |
| Turbulent Wall Functions | Scalable |

| Domain - Solid | |
|---|---|
| Type | Solid |
| Location | Solid |
| Settings | |
| Domain Motion | Stationary |
| Domain Interface - Domain Interface 1 | |
| Boundary List1 | Domain Interface 1 Side 1 |
| Boundary List2 | Domain Interface 1 Side 2 |
| Interface Type | Fluid Solid |
| Settings | |
| Interface Models | General Connection |
| Heat Transfer | Conservative Interface Flux |
| Mesh Connection | Automatic |

Boundary Physics for CFX

| Domain | Boundaries | |
|---|---|---|
| Fluid | Boundary - Inlet | |
| | Type | INLET |
| | Location | Inlet |
| | Settings | |
| | Flow Regime | Subsonic |
| | Heat Transfer | Static Temperature |
| | Static Temperature | 6.0000e+02 [K] |
| | Mass And Momentum | Normal Speed |
| | Normal Speed | Inlet Velocity |
| | Turbulence | Medium Intensity and Eddy Viscosity Ratio |
| | Boundary - Domain Interface 1 Side 1 | |
| | Type | INTERFACE |
| | Location | FS Interface |
| | Settings | |
| | Heat Transfer | Conservative Interface Flux |
| | Mass And Momentum | No Slip Wall |
| | Wall Roughness | Smooth Wall |
| | Boundary - Outlet | |
| | Type | OPENING |

| | | |
|---|---|---|
| | Location | Outlet |
| | Settings | |
| | Flow Regime | Subsonic |
| | Heat Transfer | Opening Temperature |
| | Opening Temperature | massFlowAve(Temperature)@Outlet |
| | Mass And Momentum | Entrainment |
| | Relative Pressure | 0.0000e+00 [Pa] |
| | Pressure Option | Opening Pressure |
| | Turbulence | Zero Gradient |
| | Boundary - Symmetry1 | |
| | Type | SYMMETRY |
| | Location | Symmetry1 |
| | Settings | |
| Solid | Boundary - Domain Interface 1 Side 2 | |
| | Type | INTERFACE |
| | Location | SF Interface |
| | Settings | |
| | Heat Transfer | Conservative Interface Flux |
| | Boundary - Symmetry2 | |
| | Type | SYMMETRY |
| | Location | Symmetry2 |
| | Settings | |
| | Boundary - Inlet Wall | |
| | Type | WALL |
| | Location | Inlet Wall |
| | Settings | |
| | Heat Transfer | Fixed Temperature |
| | Fixed Temperature | 6.0000e+02 [K] |
| | Boundary - Outer Wall | |
| | Type | WALL |
| | Location | Outer Wall |
| | Settings | |
| | Heat Transfer | Heat Transfer Coefficient |
| | Heat Transfer Coefficient | HTC |

| | | |
|---|---|---|
| | Outside Temperature | 3.0000e+02 [K] |
| | Boundary - Solid Default | |
| | Type | WALL |
| | Location | F90.119, F92.118 |
| | Settings | |
| | Heat Transfer | Adiabatic |

**LM2500 Model**

Mesh Information for CFX

| Domain | Nodes | Elements | Tetrahedra | Wedges | Pyramids | Hexahedra | Polyhedra |
|---|---|---|---|---|---|---|---|
| Fluid | 363802 | 180000 | 0 | 0 | 0 | 180000 | 0 |
| Solid | 14408 | 3600 | 0 | 0 | 0 | 3600 | 0 |
| All Domains | 378210 | 183600 | 0 | 0 | 0 | 183600 | 0 |

Mesh Statistics for CFX

| Domain | Minimum Face Angle | Maximum Face Angle | Maximum Element Volume Ratio |
|---|---|---|---|
| Fluid | 90 [ degree ] | 90 [ degree ] | 1.00012 |
| Solid | 90 [ degree ] | 90 [ degree ] | 1.0001 |
| All Domains | 90 [ degree ] | 90 [ degree ] | 1.00012 |

Domain Physics for CFX

| Domain - Fluid | |
|---|---|
| Type | Fluid |
| Location | Fluid |
| Materials | |
| Air Ideal Gas | |
| Fluid Definition | Material Library |
| Morphology | Continuous Fluid |
| Settings | |
| Buoyancy Model | Non Buoyant |
| Domain Motion | Stationary |
| Reference Pressure | 1.0000e+00 [atm] |
| Heat Transfer Model | Thermal Energy |
| Include Viscous Dissipation Term | On |
| Turbulence Model | k epsilon |

| | |
|---|---|
| Turbulent Wall Functions | Scalable |
| Domain - Solid | |
| Type | Solid |
| Location | Solid |
| Settings | |
| Domain Motion | Stationary |
| Domain Interface - Domain Interface 1 | |
| Boundary List1 | Domain Interface 1 Side 1 |
| Boundary List2 | Domain Interface 1 Side 2 |
| Interface Type | Fluid Solid |
| Settings | |
| Interface Models | General Connection |
| Heat Transfer | Conservative Interface Flux |
| Mesh Connection | Automatic |

Physics for CFX

| Domain | Boundaries | |
|---|---|---|
| Fluid | Boundary - Inlet | |
| | Type | INLET |
| | Location | Inlet |
| | Settings | |
| | Flow Regime | Subsonic |
| | Heat Transfer | Static Temperature |
| | Static Temperature | 6.0000e+02 [K] |
| | Mass And Momentum | Normal Speed |
| | Normal Speed | Inlet Velocity |
| | Turbulence | Medium Intensity and Eddy Viscosity Ratio |
| | Boundary - Domain Interface 1 Side 1 | |
| | Type | INTERFACE |
| | Location | FS Interface |
| | Settings | |
| | Heat Transfer | Conservative Interface Flux |
| | Mass And Momentum | No Slip Wall |
| | Wall Roughness | Smooth Wall |
| | Boundary - Outlet | |

| | | |
|---|---|---|
| | Type | OPENING |
| | Location | Outlet |
| | Settings | |
| | Flow Regime | Subsonic |
| | Heat Transfer | Opening Temperature |
| | Opening Temperature | massFlowAve(Temperature)@Outlet |
| | Mass And Momentum | Entrainment |
| | Relative Pressure | 0.0000e+00 [Pa] |
| | Pressure Option | Opening Pressure |
| | Turbulence | Zero Gradient |
| | Boundary - Symmetry1 | |
| | Type | SYMMETRY |
| | Location | Symmetry1 |
| | Settings | |
| Solid | Boundary - Domain Interface 1 Side 2 | |
| | Type | INTERFACE |
| | Location | SF Interface |
| | Settings | |
| | Heat Transfer | Conservative Interface Flux |
| | Boundary - Symmetry2 | |
| | Type | SYMMETRY |
| | Location | Symmetry2 |
| | Settings | |
| | Boundary - Inlet Wall | |
| | Type | WALL |
| | Location | Inlet Wall |
| | Settings | |
| | Heat Transfer | Fixed Temperature |
| | Fixed Temperature | 6.0000e+02 [K] |
| | Boundary - Outer Wall | |
| | Type | WALL |
| | Location | Outer Wall |
| | Settings | |
| | Heat Transfer | Heat Transfer Coefficient |
| | Heat Transfer Coefficient | HTC |

| | | |
|---|---|---|
| | Outside Temperature | 3.0000e+02 [K] |
| | Boundary - Solid Default | |
| | Type | WALL |
| | Location | F90.119, F92.118 |
| | Settings | |
| | Heat Transfer | Adiabatic |

THIS PAGE INTENTIONALLY LEFT BLANK

# LIST OF REFERENCES


[1] United States Department of the Navy, “Strategy for Renewable Energy,” 2012.

[2] S. Sathe and K. Millsaps, *WHRS Program Roadmap 2014–2020*, Monterey: NPS.

[3] C. H. E. Koh, “Performance and reliability of exhaust gas waste heat recovery units,” M.S. thesis, Mech. Eng. Dept., Naval Postgraduate School, Monterey, CA, 2014.

[4] J. Kuseian, “Naval Power Systems Technology Development Roadmap PMS 320,” PMS 320 Electric Ships Office, 2013.

[5] United States Marine Corps, “Marine Corps Expeditionary Energy Office,” 2015. [Online]. Available: http://www.hqmc.marines.mil/e2o/E2OHome.aspx. [Accessed 6 May 2015].

[6] F. P. Incropera and D. P. DeWitt, *Introduction to Heat Transfer.* Hoboken, NJ: Wiley, 2002.

[7] F. A. Di Bella, “SBIR Project # N103: Gas Turbine Engine Exhaust Waste Heat Recovery Shipboard Module Development using Supercritical Carbon Dioxide (S-CO2) Brayton Cycle with Thermoelectric Generator Technology,” Naval Sea Systems Command, 2011.

[8] R. N. V. Dolz, A. Garcia and J. Sanchez, “HD diesel engine equipped with a bottoming Rankine cycle as a waste heat recovery system. Part 1: Study and analysis of the waste heat energy,” *Appl. Therm. Eng.*, vol. 36, pp. 269–278, 2012.

[9] B. Kilkovsky, P. Stehlik, Z. Jegla, L. L. Tovazhnyansky, O. Arsenyeva and P. O. Kapustenko, “Heat exchangers for energy recovery in waste and biomass to energy technologies–I. Energy recovery from flue gas,” *Appl. Therm. Eng.*, vol. 64, pp. 213–223, 2014.

[10] C. Yu and K. T. Chau, “Thermoelectric automotive waste heat energy recovery using maximum power point tracking,” *Energy Conv. Manag*, vol. 50, pp. 1506–1512, 2009.

[11] F. A. Di Bella, “Gas turbine engine exhaust waste heat recovery navy shipboard module development,” in *Supercritical CO2 Power Cycle Symposium*, Boulder, CO, 2011.

[12] F. A. Di Bella. “Super Critical CO2 Power Cycle Symposium.” 2011. [Online]. Available: http://www.sco2powercyclesymposium.org/resource_center/system_concepts/gas-turbine-engine-exhaust-waste-heat-recovery-navy-shipboard-module-development. [Accessed 25 April 2015].

[13] FLIR Commerical Vision Systems B.V. “Seeing through fog and rain with a thermal imaging camera: Metrological effects of Fog & Rainupon IR Camera Performance.” n.d.. [Online]. [Accessed 1 August 2014].

[14] A. Birk and W. Davis, “Suppressing the infrared signatures of marine gas-turbines,” *J. Eng. Gas. Turbines Power-Trans. ASME,* vol. 111, pp. 123–129, 1989.

[15] A. Birk and D. Vandam, “Infrared signature suppression for marine gas-turbines–Comparison of sea trial and model test-results for the Dres Ball Irss system,” *J. Eng. Gas. Turbines Power-Trans. ASME,* vol. 116, pp. 75–81, 1994.

[16] Z. Du, F. Zhong and Y. Zhao, “Effect of scale factor on infrared radiation characteristics of marine exhaust system with infrared signature suppression device and its correction,” *Journal of Infrared and Millimeter Waves,* vol. 20, pp. 437–441, 2001.

[17] J. A. Guarnieri and P. G. Cizmas, “A method for reducing jet engine thermal signature,” *International Journal of Turbo & Jet-Engines,* vol. 25, pp. 1–11, 2008.

[18] H. Schleijpen and F. Neele, “Ship exhaust gas plume cooling,” *Targets and Backgrounds X: Characterization and Representation,* vol. 5431, pp. 66–76, 2004.

[19] Z. Wei, Y. Qing-qing, L. Shi-peng and W. Ning-fei, “Numerical study on the influence of aluminum on infrared radiation signature of exhaust plume,” in *International Symposium on Photoelectronic Detection and Imaging 2013: Infrared Imaging and Applications*, 2013.

[20] M. Beale, “Turning vanes in exhaust duct flow: study for energy efficiency, optimization and pressure drop mitigation,” M.S. thesis, Mech. Eng. Dept., Naval Postgraduate School, Monterey, 2014.

[21] ANSYS, Inc., *ANSYS CFX-Solver Theory Guide.* Canonsburg, PA: ANYS, Inc., 2013.

[22] ANSYS, Inc., *ANSYS CFX-Solver Modeling Guide.* Canonsburg, PA: ANSYS, Inc., 2013.

[23] R. K. Shah and A. L. London, *Laminar Flow Forced Convection in Ducts*. New York: Academic Press, 1978.

[24] R. K. Shah and M. S. Bhatti, “Laminar convective heat transfer in ducts,” in *Handbook of Single-Phase Convective Heat Transfer*. New York, John Wiley & Sons, 1987, pp. 3.1–3.137.

[25] C.-L. Hwang and L.-T. Fan, “Finite difference analysis of forced-convection heat transfer in entrance region of a flat rectangular duct,” *Applied Science Research,* vol. 13, no. A, pp. 401–422, 1963.

[26] K. Stephan, “Wärmeübergang und druckabfall bei nicht ausgebildeter Laminarströmung in Rohren und in ebenen Spalten,” *Chem. -Ing. -Tech,* vol. 31, pp. 773–778, 1959.

[27] S. D. Joshi and R. K. Shah, “Convective heat transfer in bends and fittings,” in *Handbook of Single-Phase Convective Heat Transfer*. New York, John Wiley & Sons, 1987, pp. 10.1–10.32.

[28] S. R. Tailby and P. W. Staddon, “The Influence of 90 degree and 180 degree Pipe Bends on Heat Transfer from an Internally Flowing Gas Stream,” *Heat Transfer 1970,* Paper No. FC 4.5, 1970.

[29] H. Yamashita, R. Izumi, G. Kushida and T. Mizuno, “Fluid Flow and Heat Transfer in a Two-dimensional Miter-bend,” *Bullentin of JSME, The Japan Society of Mechanical Engineers,* vol. 29, no. 258, pp. 4164–4169, 1986.

[30] E. F. Schmidt, “Wärmeübergang und druckverlust in rohrschlangen,” *Chem. Ing. Tech.,* vol. 39, pp. 781–789, 1967.

[31] M. B. Hansen, “ANSYS Workbench CFX parametric setup based on Solidworks geometry,” [YouTube video], 24 June 2014. [Online]. Available: https://www.youtube.com/watch?v=fpnvNJ49FAk. [Accessed 2015 April 2015].

[32] D. L. Blunck and J. P. Gore, “Study of narrowband radiation intensity measurements from subsonic exhaust plumes,” *J. Propul. Power,* vol. 27, pp. 227–235, 2011.

**[33]** S. Heragu, K. Rao and B. Raghunandan, “Generalized model for infrared perception from an engine exhaust,” *J. Thermophys. Heat Transfer,* vol. 16, pp. 68–76, 2002.

THIS PAGE INTENTIONALLY LEFT BLANK

# INITIAL DISTRIBUTION LIST

1. Defense Technical Information Center
   Ft. Belvoir, Virginia

2. Dudley Knox Library
   Naval Postgraduate School
   Monterey, California